Rotational behavior of PEGylated gold nanorods in a lipid bilayer system

Priyanka A. Oroskar[1], Cynthia J. Jameson[1,2], and Sohail Murad[1,3]*

1. **Department of Chemical Engineering, University of Illinois at Chicago, 810 S. Clinton Street, Chicago, Illinois 60607, United States**
2. **Department of Chemistry, University of Illinois at Chicago, 845 West Taylor Street, Chicago, Illinois 60607, United States**
3. **Department of Chemical and Biological Engineering, Illinois Institute of Technology, 3300 S. Federal Street, Chicago, Illinois 60616, United States**

ABSTRACT:

PEGylated gold nanorods are widely used as nanocarriers in targeted drug delivery and other nanotechnology applications due to the special optical and photo-thermal characteristics of gold nanorods. In this work, we employ coarse-grain molecular simulations to examine the pathway by which PEGylated gold nanorods enter and exit a DPPC lipid bilayer membrane and follow the behavior of the system to investigate the consequences. We find that PEGylated gold nanorods rotate during permeation, lying down and straightening up as they make their way through the lipid membrane. We find that this rotational behavior, irrespective of the initial orientation of the nanorod with respect to the membrane normal, is concomitant with the changing interactions of PEG beads with lipid head beads in both membrane leaflets. For a nanorod with hydrophilic ligands, such as PEG, lying down appears to be driven by favorable hydrophilic interactions with the phosphate and choline groups of the lipid. Mobility of the ligands offers mechanisms for these favorable interactions and for minimizing unfavorable interactions with the hydrophobic lipid tails that constitute the inner section of the membrane; the PEG ligands can stretch out to reach the phosphate and choline groups of both leaflets and they can coil in and interact with each other and avoid the alkane lipid tails. Recently developed experimental techniques for imaging, orientation, and rotation of single gold nanorods may be able to observe this predicted rotational behavior. We find that lipid flip-flop mechanisms do not differ significantly from a spherical gold nanoparticle to a gold nanorod, and PEGylated gold nanorods like their spherical counterparts do not remove lipid molecules from the bilayer membrane. Our results should be of interest to experimentalists who plan to use functionalized gold nanorods in biomedical applications.

Keywords: drug delivery, gold nanorod, polyethylene glycol (PEG), molecular dynamics, coarse-grained

1.0 Introduction

The diversity of nanomaterials available to the drug delivery industry has given rise to nanoparticle carriers that vary in size, shape, chemical functionality, and surface charge, among other properties [1,2,3]. Several classes of nanoparticles have been found to serve as efficient therapeutic carriers for targeted drug delivery. In particular, gold nanoparticles provide the special advantages of ease of preparation and of modification of the surface with many functional groups, in addition to desirable optical properties that provide opportunities for thermal heating and imaging. Gold cores functionalized by polyethylene glycol (PEGylation) have a hydrophilic protective layer that helps to prevent the absorption of opsonin proteins, thereby limiting their recognition and clearance by macrophages, which in turn prolongs their lifetime in the circulatory system (thus was coined the term "stealth character" conferred by PEGylation) [4,5]. PEGylated AuNPs have been investigated in *in vitro* and *in vivo* studies for potential applications [6,7]. Wang et al. have demonstrated that PEG-AuNPs markedly accumulate by approximately 25-fold more in tumor tissues than in normal muscle tissue [8]. Therefore, PEG-AuNPs have valuable applications in enhancing X-ray tumor imaging and radiotherapy and have a great potential for customized cancer therapy [9,10]. For example, the possibility of biologically specific X-ray imaging in living animals is indicated by the report on PEGylated AuNPs conjugated to anti-CD4 monoclonal antibodies that provides molecularly selective X-ray contrast enhancement of peripheral lymph nodes in living mice by Eck et al. [11]. Although PEGylated AuNP have been shown to have very low cytotoxic effect on many cell lines [12], Huang et al. have demonstrated that PEGylated gold nanoparticles induce apoptosis in a particular type of leukemia cells, human chronic myeloid leukemia cells. Their results indicated that PEG-AuNPs markedly inhibited the viability and impaired the cell membrane integrity of these cells. The particles caused morphological changes and other indicators typical of cell death [13]. In a recent review article [14], the delivery process of nanoparticles into cells was explained in detail. Nanoparticles inserted into the human body will make contact with proteins and other cells present, including phagocytic cells,

which remove foreign bodies from the bloodstream. Once the nanoparticle has escaped the clearance by the immune system, it will reach the targeted tissues or cells and ultimately make contact with the cell membrane first. Accordingly, it is necessary to assess the damage functionalized nanocarriers may cause to membranes of non-targeted cells present *in vivo* since loss of integrity to cell membranes can result in cytotoxic environments and cell apoptosis.

Shape is an important property of nanoparticles and it is believed that shape can play a role in therapeutic delivery processes [15]. Gold nanorods, rod-shaped gold nanoparticles, have been featured prominently in new therapies. Blood vessels located near tumors have tiny pores just large enough for the nanorods to enter; nanorods accumulate in the tumors, and within three days, the liver and spleen clear any that don't reach the tumor [16,17,18]. Furthermore, gold nanorods have unique optical properties different from spherical AuNPs [19,20]. That is, they show two surface plasmon bands corresponding to the transverse and longitudinal surface plasmon bands in the visible (~ 520 nm) and the near-infrared regions, respectively. The longitudinal band has a substantially larger extinction coefficient than the transverse band. Thus, gold nanorods are unusual materials with an intense surface plasmon band that affords absorption, fluorescence [21,22], and light scattering [23,24] in the visible and near infrared region, and inducing two-photon luminescence [25].

Plasmon-resonant gold nanorods, which have large absorption cross-sections at near-infrared (NIR) frequencies, are excellent candidates as multifunctional agents for image-guided therapies based on localized hyperthermia. Hyperthermia, in which biological tissues are exposed to higher than normal temperatures, is currently under consideration as a noninvasive approach to cancer therapy, since tumor cells are considered to be more susceptible to hyperthermic effects than healthy cells due to their higher metabolic rates. Numerous clinical studies have demonstrated a marked reduction in tumor size after treatment by localized hyperthermia. One promising approach is to introduce photo-thermal agents in the form of anisotropic (nanorod) gold nanoparticles, which can support plasmon resonances with very high absorption cross-sections at near-IR wavelengths [26,27,28,29]. Another application of gold nanorods is in imaging. Emitting two-photon luminescence signals that are sufficiently intense for single-particle detection, due to their

large two-photon absorption cross sections at longitudinal plasmon resonance, permits the direct imaging of nanorods in biological samples.

To apply gold nanorods to medical fields including tumor imaging, photothermal therapy, gene delivery, and drug delivery, efficient delivery of nanorods to a specific site after systemic injection is key. For the targeted delivery *in vivo*, a "stealth character" is required, as mentioned above, which is provided by PEGylation. Gold nanorods modified with polyethylene glycol (PEG) were prepared for the first time by Nidome et al.; they then evaluated its cytotoxicity *in vitro* and bio-distribution after intravenous injection into mice. In this study, PEG-modified gold nanorods were found to have long lasting circulation in the blood [30], and low cytotoxicity (although the conditions under which this is true is still under debate), an essential property for medical application. From analysis of biodistribution of gold nanorods after intravenous injection, PEG-modified gold nanorods were found stably circulating in blood with a half-life of approximately 1 h, and there was no accumulation in major organs except for the liver at least for 72 h. Using polyethylene glycol (PEG)-coated gold nanorods, Lin et al. quantitatively evaluated the ability of nanoparticles to penetrate and accumulate in sarcomas through passive targeting mechanisms. They demonstrated in a genetically engineered mouse model of sarcoma, which accurately mimics the human disease in terms of structure and biology, that PEG-NR–mediated photothermal heating results in significant delays in tumor growth with no progression of the cancer in some instances [31,32].

These applications provide our motivation to consider the mechanism by which PEGylated gold nanorods interact with and permeate a model membrane. Our previous studies have focused on understanding permeation of a lipid bilayer by a spherical gold nanoparticle decorated with alkanethiol ligands [33] and more recently, PEG ligands [34], which improve the stability and solubility of the functionalized nanoparticle *in vivo* [35,36,37]. In the current study, we investigate the mechanism of penetration of PEGylated nanorods, designed so the core has the same volume as the core of the spherical PEG-AuNPs used in our previous study, into the lipid membrane bilayer, the dependence of the permeation pathway on the degree of alignment of the nanorod axis with the normal to the bilayer, and the contribution of the interactions between the sites representing the hydrophilic PEG and all components of the lipid molecules including the hydrophilic

phosphate, choline, and glycerol heads and the hydrophobic tails of the lipids in the bilayer membrane to the permeation process. Our results may be of interest to biomedical engineers and other experimentalists who intend to utilize gold nanorods with biocompatible surface modifications for a variety of drug delivery applications.

2.0 Methods

2.1 Coarse-grained model

In order to study the behavior of PEGylated nanorods (NRs) as they permeate lipid membranes, we utilize molecular dynamics simulations or 'computer experiments' for the investigation. We have used a coarse-grained (CG) representation of a DPPC lipid bilayer for a model membrane [38], and a coarse-grained model of PEG represents the ligands in our functionalized gold nanorod [39]. DPPC phospholipids membranes are validated against experiments frequently in molecular dynamics simulations [40,41] and are of interest to research groups since they hold biological importance acting as an integral part of pulmonary surfactants [42] and other entities such as lipid rafts [43]. DPPC is fairly rigid maintaining a tightly packed orientation compared to other phospholipid bilayers [44]; our studies on DPPC phospholipid bilayers can aid experimentalists in understanding effects of nanoparticle permeation on other phospholipid bilayers of similar rigidity. Coarse-grained models differ from atomistic representations where each atom is treated as an interaction site. In coarse-grained models, the degrees of freedom in a system are reduced by grouping small clusters of atoms into one interaction site. The reduction of number of interaction sites allows coarse-grained simulation models to be more efficient than atomistic simulations as they permit longer time scales for study. Coarse-grained molecular dynamics simulations have been used frequently to study various biomolecular systems, many of which are larger than the one in the present study [45,46]. The behavior of PEG molecules in solvent has been explored using molecular dynamics as well [47,48,49].

We adopt the MARTINI coarse-grained force field developed by Marrink and colleagues [50] and use their interaction parameters between sites in our system. The MARTINI coarse-grained force field has been established to accurately reproduce semi-quantitatively

the fundamental structural and thermodynamic properties of biomolecules such as proteins and amino acids as well as lipid membranes [51]. Coarse-grained models cannot reproduce all details that can be elucidated at the atomistic level however for the permeation consequences that we are exploring, the results from the coarse-grained level details can be considered a realistic representation. Previously, we showed that the lipid translocation mechanism observed as a consequence of gold nanoparticle permeation is the same mechanism observed in atomistic simulations by Gurtovenko and co-workers [52,53]. In addition, several groups have employed the MARTINI model to study PEG and the interaction of PEG and PEO polymers with lipid molecules and found good agreement with experimental studies [54,55,56]. Our present lipid bilayer and PEGylated AuNR system contains charged, bonded and non-bonded interactions, all, which are characterized with unique interaction parameters specific to the type of interaction site. The MARTINI coarse-grained force field consists of a comprehensive library of pre-tested interaction parameters depending on 4 types interaction sites; polar (P-type), non-polar (N-type), apolar (C-type), and charged (Q-type). We assign MARTINI P4-type interactions sites for water molecules and C5-type for the gold atoms. We use the traditional MARTINI model for water where four water molecules are mapped as one CG water bead. Particle pairs which are designated as having non-bonded interactions are described by a shifted Lennard-Jones (LJ) potential energy function. Most non-bonded particle pairs in the MARTINI coarse-grained model are typified with an effective distance of σ_{ij} = 0.47 nm, while interactions between charged or apolar-type sites are characterized with an effective distance of σ_{ij} = 0.62 nm. ε_{ij}, the LJ potential well depth, is an adjusted parameter based on the type of interacting particle pairs where ε_{ij} = 2.0–3.1 kJ/mol is designated for interactions between polar and non-polar site types. Particle pairs considered to be non-polar or strongly polar as with aliphatic chains are described by ε_{ij} ranging from 3.5-5.6 kJ/mol.

Interactions between charged particle pairs are modeled using the shifted Coulombic potential energy function. We neglect long-ranged electrostatic pairwise interactions beyond 1.2 nm. In the MARTINI coarse-grained force field, interactions between bonded particle types are characterized with the weak harmonic potential energy function described.

Our systems include bonded interaction sites that describe complex chemical structures and must include bond angles and dihedral angle information to more accurately represent the bond configuration. Bond angles are characterized by a weak harmonic potential function of cosine type where

$$V_{angle}(\theta) = \frac{1}{2}K_{angle}[\cos(\theta) - \cos(\theta_0)]^2 \quad (1)$$

and dihedral interactions between quadruplets of atoms such as in PEG are represented in the MARTINI coarse-grained force field by a dihedral potential function.

In our simulations, we use a methyl-terminated form of PEGn (often referred to as Peon) which contains 'n+1' number of coarse-grained beads compared to PEGn with only 'n' number of coarse-grained beads as described by the MARTINI model. The original coarse-grained model of PEG and PEO developed by Lee and co-workers [57] considered a harmonic potential function with angle potential of the cosine-type (Equation (1)) and force constant of 85 kJ/mol. More recently, it was determined by Lee and Pastor [58] that numerical stability improved when an alternative potential function described by Equation (2) was used with a force constant of 50 kJ/mol.

$$V_{angle}(\theta) = K_{angle}[\theta - \theta_0]^2 \quad (2)$$

Thus, we use Equation (2) rather than Equation (1), and validate our modification against the original MARTINI model. Critical parameters that have been used customarily [59] to describe behavior of polymers are radius of gyration R_g and root mean square end-to-end distance ($<R_{ee}>$). In the original coarse-grained MARTINI model of PEG [57], single PEG chains of different lengths were each placed in a 10x10x10 Å simulation box with approximately 9200 previously equilibrated coarse-grained water molecules. The simulation was run for 400 ns at 296 K and pressure was maintained at 1 bar with the NPT ensemble time integrator. In obtaining the R_g and $<R_{ee}>$ values, data was averaged from 4 simulations with different initial conditions with the first 20 ns of data omitted. We repeated these particular simulations for a PEG9 chain with the updated parameters and

Equation (2) and obtained R_g and $<R_{ee}>$ of 6.4 Å ± 0.03 and 14.69 Å ± 0.17, respectively, which are in acceptable agreement with their original values of 6.3 Å ± 0.1 and 15.7 Å ± 0.1, respectively

2.2 Simulated PEGylated NRs with various lengths of PEG

As in our previous studies where a 3.0 nm in diameter gold nanoparticle (AuNP) was obtained by cutting a nearly spherical structure from a bulk face-centered-cubic (FCC) lattice of gold atoms, we have cut a cylindrical rod from the same FCC lattice of gold atoms to construct a gold nanorod (AuNR). For comparison with our previous work [34], we choose the volume of the nanorod core to be identical to the spherical core. Thus, we use a gold nanorod which has the same volume as that of the 3.0 nm diameter spherical AuNP with aspect ratio of 2.2. Aspect ratios of gold nanorods synthesized experimentally for biomedical applications range from 1 to 5 [60,61]. We use the same procedure as for our previous work [34] to condense the PEGn-SH ligands onto the surface of the nanorod, i.e. a cycled annealing simulation procedure, where the gold nanorod was immersed in polymer melts, mimicking experimental studies where polymer nanocomposites containing polystyrene or polyethylene oxide are doped with nanoparticles or nanorods [62,63,64,65,66]. In principle, the interaction parameters of Au atoms on the surface of a nanorod should depend on the number of nearest Au neighbors the atom has. For a sphere, all Au surface atoms are equivalent but for a nanorod this is not true. The majority of the Au atoms are on the curved cylinder wall but the Au atoms, which constitute the bases, and the circular edges are not equivalent to the former. For simplicity, we ignore such subtleties and assign the same interaction parameter for the Au atoms on the surface as we have used for the spherical core AuNP. In accordance with our previous work in constructing a PEGylated AuNP with various lengths of PEG, we employed the same cycled annealing protocol for to the gold nanorod, starting with PEG3-SH ligands and obtained a PEGylated AuNR with coverage density of 2.01 ligands/nm^2. We previously demonstrated that it is not accurate to assume that coverage density is independent of ligand length [34]. Subsequently, it has been found in experimentally synthesized PEGylated nanoparticles that the coverage density of PEG on functionalized nanoparticles decreases as the chain

length or molecular weight increases [67]. Experimental work by Rahme et al. [68] corroborated these findings where it was observed that the grafting density of the mPEG-SH ligands on a spherical gold nanoparticle 15 nm in diameter decreased from 3.93 to 0.31 PEG nm^{-2} as the molecular weight of the ligands increased from 2100 up to 51400 g mol^{-1}, respectively. Rahme and colleagues attributed this to increased steric hindrance and polymer conformational entropy with increase in the PEG chain length.

After repeating the cycled annealing procedure with our replacement technique (described in detail in our previous work [34]), we obtained PEG6, PEG12, and PEG18 AuNR's with coverage densities of 1.54, 0.88, and 0.56 ligands/nm^2, respectively, which are lower than the coverage densities of the respective spherical AuNP of the same core volume. Our PEG6 and PEG12 spherical gold nanoparticles had somewhat higher surface coverages of 1.66 ligands/nm^2 and 1.06 ligands/nm^2, respectively. Indeed, PEGylated AuNRs (with aspect ratio of approximately 3.6) synthesized experimentally under the same conditions have been found to have much lower coverage densities overall than their spherical counterpart AuNPs (e.g. 0.052 ligands/nm^2 compared to 1.63 ligands/nm^2, respectively) [69]. However, Kinnear and co-workers utilized a two-step reaction to synthesize a PEGylated AuNR of aspect ratio 3.2 with higher surface coverage of 0.89 ligands/nm^2 [70.] It has been rationalized that smaller nanorods such as this exhibit higher surface curvature and can allow for increased ligand packing to occur on the surface due to reduced steric contacts between grafted polymers [71,72]. For our permeation studies, we choose the PEG12 and PEG18 AuNRs since both have grafting densities comparable to Kinnears experimental values.

After cycled annealing, we introduced the equilibrated PEG12-NR and PEG18-NR into a simulation box with previously equilibrated water molecules by removing the water molecules that would have overlapped with the nanoparticle. We then equilibrated the PEGylated nanorods in this system for 200 ns in order to allow the PEG ligands to explore multiple conformations. Similar to our work on spherical PEGylated gold nanoparticles [34], we observed the PEG ligands to exhibit a distribution of configurations from coiled close to the nanoparticle surface to stretched out away from the nanoparticle. In the nanoparticle melt, a majority of the PEG ligands are stretched out while a few remain coiled close to the nanoparticle surface; in the presence of water more PEG ligands are found to

be coiled while few are found to be stretched out. Other groups who have simulated PEG itself in water utilizing polarizable water models have also observed coiling of PEG polymers [73].

2.3 Simulation of permeation of a PEGylated AuNR in a lipid bilayer membrane

The lipid bilayer membrane system is 12.8x12.6x30.0 nm in size and consists of a dipalmitoylphosphatidylcholine (DPPC) membrane with 512 DPPC molecules and approximately 33,600 CG water molecules. In previous investigations, we have observed that this lipid membrane self-assembles from an isotropic solution of DPPC lipid molecules and water in a coarse-grained simulation at 323 K [74]. It is known that the MARTINI force field and coarse-grained type simulations accelerate and influence the self-assembly process however, lipid membrane self-assembly is a realistic process that occurs spontaneously in biological systems [75,76]. Properties of this self-assembled DPPC lipid bilayer e.g. thickness of the membrane and area per lipid are in good agreement with experimental measurements, which validates the efficacy of the CG model to represent a lipid membrane [74]. Experimental investigations of permeation in lipid membranes have utilized phospholipid molecules maintained on solid supports that mimic the role of the extracellular membrane matrix *in vivo* [77]. Consequently, to replicate these experimental permeation studies more closely in our molecular simulation, we tethered roughly 8% of the boundary lipid molecules (1 nm from the edge of the membrane) to their initial position using a harmonic spring force. Tethering a small number of the boundary lipid molecules ensures that the lipid membrane does not translate during simulated nanoparticle permeation.

We have used external forces in the range of 70-500 pN to drive the permeation of functionalized nanoparticles into the lipid membrane. These applied external forces are significantly smaller than the forces present between nanoparticles and cell membranes (50-1200 pN) [78] and between nanoparticles (0-12 nN) [79]. Our computational experiments mimic real biomedical applications of targeted drug delivery methods where gold nanorods are injected intravascularly for therapeutic applications [80,81]. The typical flow velocity in an artery ranges from 0.15-0.2 m/s where nanocarriers that are 10-100 nm

in diameter can readily be transported during blood circulation [82,83,84]. Velocities explored in our studies are three times smaller than typical flow velocities of particles carried in the bloodstream and thus our computational experiments represent realistic scenarios where nanocarriers may come in contact with biological media and penetrate lipid membranes during circulation *in-vivo*. The thermal velocities of lipid, water, and ion molecules in our system range from 96.6-334.5 m/s and 3.0-4.0 m/s for functionalized nanoparticles. The nanoparticle velocities examined (resulting from applied forces) are several orders of magnitude smaller than these thermal velocities.

In our simulations, we will examine a PEGylated AuNR pulled (by its center-of-mass) across the lipid membrane under constant velocity, effectively representing an experiment where a functionalized gold nanorod permeates from the extracellular (Figure 1 compartment 1) to the intracellular space (Figure 1 compartment 2). All permeation simulations in the present work were performed using the LAMMPS [85] simulation package where a time-step of 10 fs was employed and a Langevin thermostat was applied with a NVE ensemble time integrator to maintain the temperature at 323 K. We realize the functionalized nanorod is quite large and may cause strong disruptions to the lipid membrane however, our membrane only occupies approximately 20% of the total system volume and therefore, we believe it is not sensitive to NVE ensemble chosen for our studies. We had previously explored consequences of permeation such as water leakage and lipid flip-flop, which have been observed in simulations with the NVE ensemble time integrator, however others have explored water pore formation and ion leakage and lipid flip-flop using the NPT ensemble time integrator [86]. Our model system mimics a solid supported membrane for which the NVE ensemble type integrator is more appropriate.

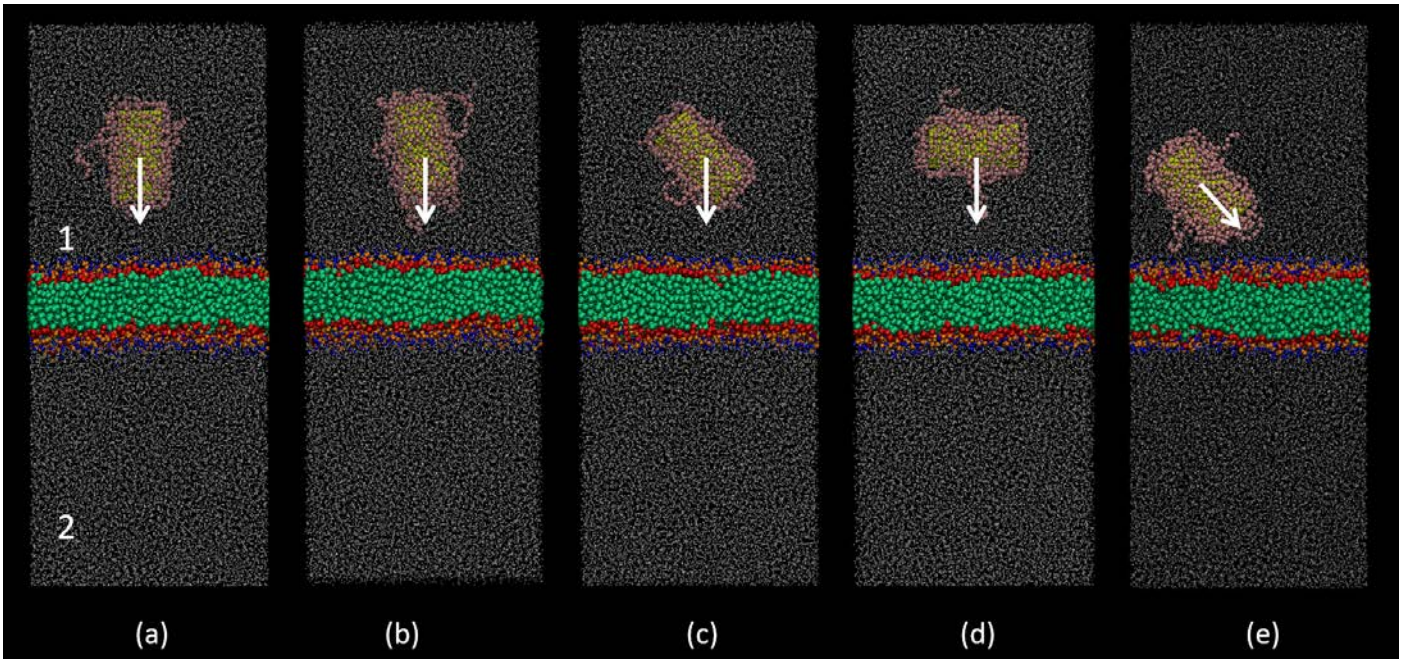

Figure 1. DPPC lipid bilayer membrane simulation system for investigation of PEGylated gold nanorod permeation from the top compartment (1) to the bottom compartment (2) across the lipid bilayer membrane where the initial angle to the membrane is varied by (a) Method (A0) = 0°, (b) Method (A1) = 10°, (c) Method (A2) = 45°, and (d) Method (A3) = 90° and (e) Method (B2) = 45° (blue = choline, orange = phosphate, red = glycerol, green = lipid tails, white = water, gold = nanorod core, pink = PEGn-SH ligands).

There are unique aspects to permeation by a nanorod particle that differ from permeation by a spherical core nanoparticle. The most significant is the entry angle, the initial angle between the nanorod long axis and the membrane surface. In our simulations, the center-of-mass of the nanorod is moved at a constant velocity towards the membrane surface; this allows the nanorod to rotate about its center-of-mass during the simulation. One approach, Method (A) (Figure 1(a)-(d)) is moving the center-of-mass of the nanorod along the direction normal to the membrane surface; we vary the initial angle of the nanorod axis relative to the membrane to explore the effects of the initial angle on permeation. In another approach Method (B) (Figure 1 (e)), we fix the ratio of the normal and transverse velocity component that is used to move the center-of-mass towards the membrane surface, while keeping the absolute velocity constant, again permitting rotation about the center-of-mass. We investigate various velocity vectors for the translation of the center-of-mass to see the effect on the permeation event. For each of these Methods, we

explore a range of constant velocities and a selection of initial angles for Method (A) and a selection of pulling velocity vectors, starting with 45°, for Method (B). Experimental studies indicate that the entry angle of PEGylated nanorods relative to the lipid membrane surface affects their internalization rate [87]. In our studies, we investigate the molecular mechanism by which this dependence on angle of entry occurs.

In all simulations, the rigid nanorod is pulled at a constant velocity by its center-of-mass. This method allows the nanorod to rattle during permeation of the membrane and rotate according to forces in the system. This represents the most natural way of penetrating the membrane as opposed to artificially holding the nanorod at 0° to the membrane throughout the process and not allowing it to fluctuate freely. The PEG ligands attached to the nanorod are flexible and move freely throughout the permeation.

In Method (A) we varied several parameters to compare permeation of the PEGylated AuNRs. We tested several translation velocities of 0.05, 0.075, 0.1, and 0.2 m/s, which will be referred to as V1, V2, V3, and V4, respectively. These velocities are the same magnitude velocities studied with our spherical PEGylated NP. We varied the initial orientation of the nanorod in the system by choosing the various initial tilt angles of the axis of the core nanorod relative to the normal to the membrane surface. In Figure 1, we show snapshots of the starting points for our systems where we vary the starting tilt angle of the nanorod axis at 0°, 10°, 45°, and 90° (parallel to the membrane). In the subsequent figures, these initial angles for the PEG18-NR will be referred to as A0, A1, A2, and A3, respectively. In Method (B) we studied a system where the PEG12-NR tilted at 45° is placed near the left boundary of the system (Figure 1(e)) and pulled at a constant absolute velocity while maintaining the angle of the velocity vector at 45° (this is referred to as B2 in the subsequent plots). Our findings from Method (A) demonstrated that the permeation pathways of PEG12-NR and PEG18-NR were similar and thus chose to study only the PEG12-NR by Method (B). Our focus in the present work is on investigating the accessible routes of penetration of a PEGylated nanorod given various possibilities for entry angle, and not on comparing effects of grafting densities and ligand lengths on certain consequences of permeation, since we have already investigated these in our previous work on spherical PEGylated AuNPs [34].

3. Permeation pathway of PEGylated NRs through a lipid bilayer membrane

Our results provide a consistent scheme for the permeation pathway of a PEGylated gold nanorod through a lipid bilayer membrane. The trajectories resulting from our simulations clearly show similarities irrespective of entry angle, but also differences. We summarize the observations of the change the change in the angle of tilt of the axis of the nanorod relative to the z-axis, the normal to the plane of the membrane surface for the smallest pulling velocity in Figure 2. In this figure, we have arbitrarily chosen to denote the entry and exit of the nanorod by marking with vertical pink dashed lines the times at which the center-of-mass of the PEGylated nanorod is 2.0 nm above from the top membrane leaflet and later, when it is 2.0 nm below the bottom membrane leaflet.

We see that in the simulations with starting tilt angles of 0°, 10°, 45°, and 90°, the tilt angle progresses from the initial value through a series of changes that passes through or close to 90° (lying down, indicated by the green dashed line in Figure 2) and, eventually, as the nanorod exits the lower leaflet of the membrane, it begins to straighten up. The tilt angle upon exit can be close to 0° or 180° (signifies a half rotation-flip of top and bottom flat areas), that is, the nanorod sometimes exits pointing up or down. Cartoon representations of the orientation of the nanorod in 3-dimensional space during the permeation event is given in Figure 3, where we show the trajectories of a nanorod starting from various angles upon approach to the membrane surface. The arrow representing the functionalized nanorod in Figure 3(a)-(e) is the line through the center of the gold nanorod core along its length. The trajectory can be considered as a sequence of three events: the nanorod is adsorbed, engulfed, then released by the membrane.

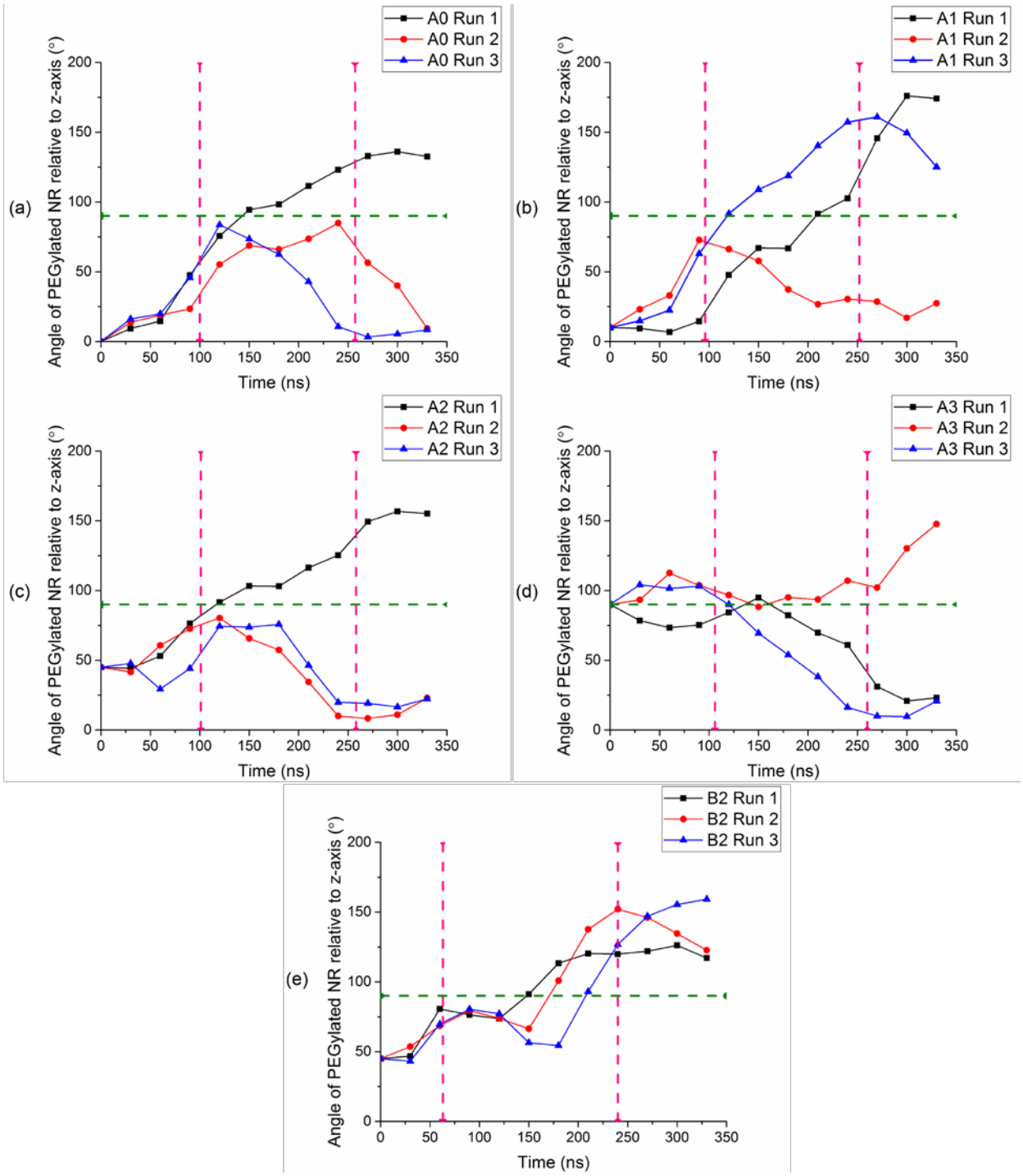

Figure 2. The tilt angle from the z-axis (normal to the membrane surface) of the nanorod axis is shown for each starting angle (a) A0 = 0°, (b) A1 = 10°, (c) A2 = 45°, (d) A3 = 90°, and (e) B2 = 45° at zero time. Data from three independent simulations are shown as individual runs. The horizontal green dashed line represents the angle at which the nanorod is perpendicular to the z-axis (in a plane parallel to the membrane surface or, lying down) and the vertical pink dashed lines represent the time when the center-of-mass of the

PEGylated nanorod is 2.0 nm above from the top membrane leaflet and later, when it is 2.0 nm below the bottom membrane leaflet.

We see in Figure 2 only the change in the tilt angle relative to the normal to the membrane surface (x-y plane), while in Figure 3, we see that the rod also turns in the x-y plane during the permeation process. For Figures 2-8, we have chosen to illustrate only the results obtained for the lowest velocity, which provides sufficient time for the interactions between the ligands and the lipids to direct the nanorod. However, the trajectories at higher pulling velocities (not shown) are similar to those in Figure 3. The cartoons in Figure 3 each represent only one example of a trajectory of the PEGylated nanorod through the lipid membrane; it is clear from Figure 2 that there are a variety of pathways available to the nanorod during the permeation. Nevertheless, every trajectory (from both Method (A) and (B)) passes through a lying down orientation at or close to 90° and straightening up upon exit at or close to 0° or 180°, not only in these examples at a pulling velocity of V1 = 0.05 m/s but also for all other pulling velocities used in this study for up to 0.2 m/s. For Method B, the direction of the velocity vector (at 45°) pulling the center-of-mass leads to a more consistent exit angle of 180°.

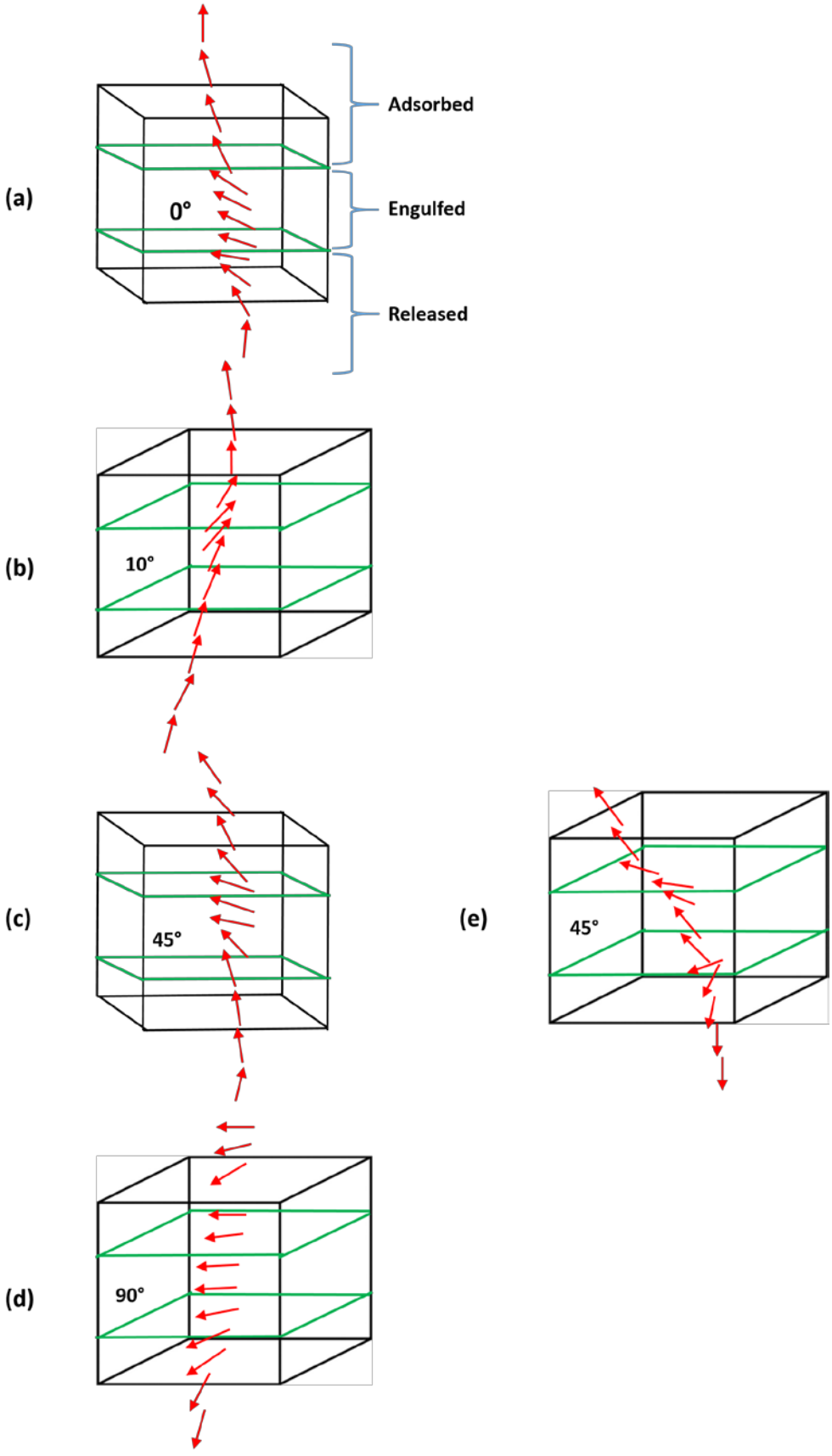
(a)
0°
Adsorbed
Engulfed
Released
(b)
10°
(c)
45°
(d)
90°
(e)
45°

Figure 3. Cartoon representation of permeation of PEG18-NR in the lipid bilayer membrane at V1=0.05 m/s and various initial angles. The green planes represent the equilibrated position of the phosphate groups in the top and bottom membrane leaflets. Initial angles are (a) A0 = 0°, (b) A1 = 10°, (c) A2 = 45°, and (d) A3 = 90° and (e) B2 = 45°. The cartoons correspond to the snapshots from Figure 4 (A1), Figure 5 (A2), Figure 6 (A3) and Figure 7 (A0), and Figure 8 (B2). Each arrow is at 30 ns intervals starting with 0 ns. The isometric view has been adjusted depending on which viewpoint gave the clearest 3-dimensional picture of the permeation pathway for the functionalized nanorod.

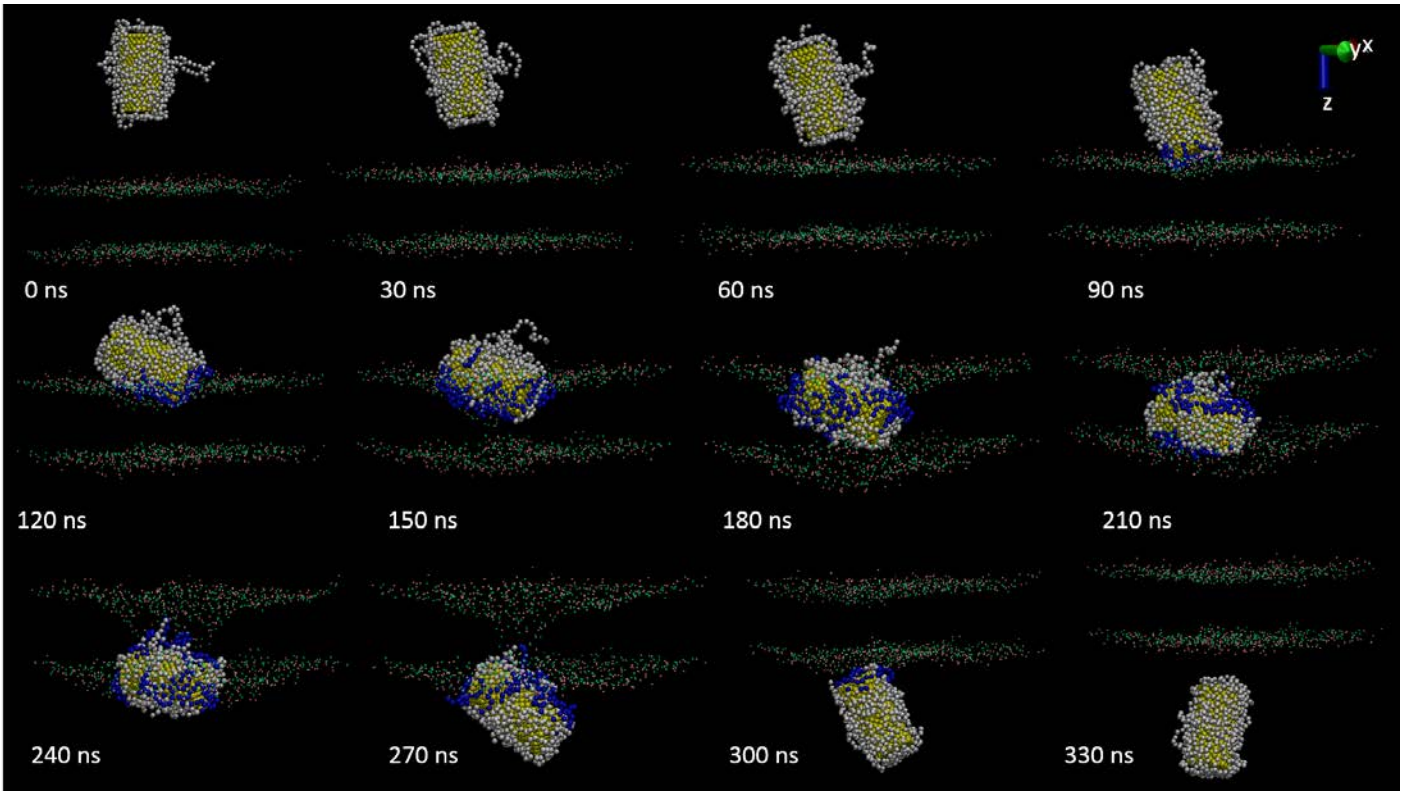

Figure 4. Molecular snapshots of permeation of PEG18-NR in the lipid bilayer membrane at V1=0.05 m/s and initial angle of A0 = 0° where pink=choline, green=phosphate, yellow= AuNR core, white= PEG18-SH ligands, and blue= PEG18 beads within 1.0 nm of choline and phosphate molecules. The cartoon in Figure 3(a) shows this particular trajectory.

In the cartoon trajectories shown in Figure 3 and the snapshots from Figures 4-8, we notice a theme followed in the permeation pathway of a nanorod; As the PEGylated nanorod enters the membrane, we observe that it tilts even further until it is almost parallel to the plane of the membrane; this occurs as soon as the leading PEG ligands start to interact with the lipid head groups. Upon exiting from the membrane, the nanorod

begins to straighten up along the membrane normal as the trailing PEG ligands interact with the lipid head groups from the bottom layer of the membrane.

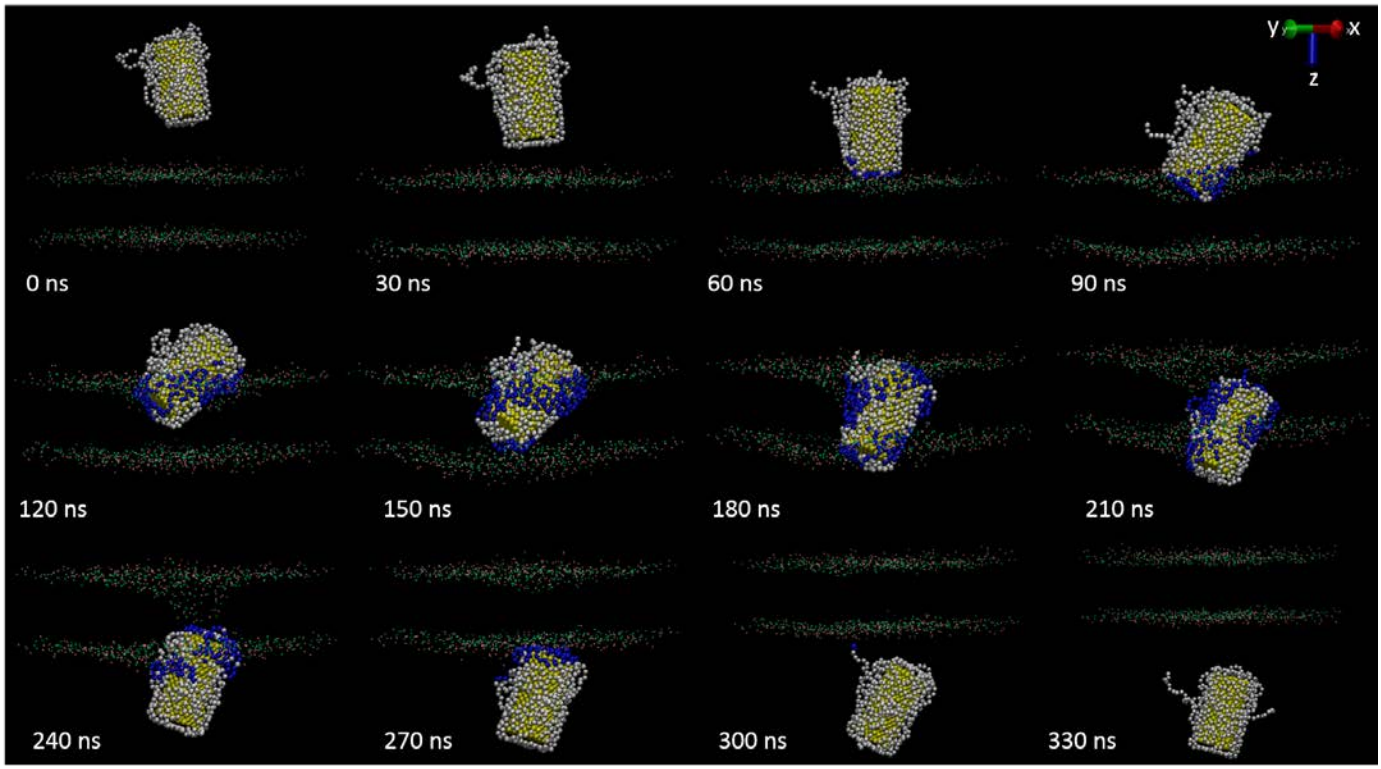

Figure 5. Molecular snapshots of permeation of PEG18-NR in the lipid bilayer membrane at V1=0.05 m/s and initial angle of A1 = 10° where pink=choline, green=phosphate, yellow= AuNR core, white= PEG18-SH ligands, and blue= PEG18 beads within 1.0 nm of choline and phosphate molecules. The cartoon in Figure 3(b) shows this particular trajectory.

It appears that the tilting of the nanorod occurs so as to maximize the favorable hydrophilic interactions between the PEG ligands and lipid head groups. At the time noted by the first pink dashed line, the PEG ligands of the nanorod have begun to interact with the hydrophilic phosphate and choline beads, causing the nanorod to lie down and the tilt angle to increase close to 90°, as seen in Figure 2, to enhance the favorable hydrophilic interactions. At the time of the second pink dashed line in Figure 2, the PEG ligands are slowly leaving the membrane with the nanorod and consequently the nanorod is straightening up on exit, i.e. a tilt angle close to 0° or 180°. We illustrate the pathway, driven in part by hydrophilic interactions of the permeating nanorod, by highlighting in blue those interactions sites on the ligand-coated nanorod that are within 1 nm of the choline and/or phosphate groups in the molecular snapshots in Figures 4-8. The cut-off for

the shifted LJ potential in our simulations is 1.2 nm. With the patch of blue on the nanorod surface constituting the number of ligand beads favorably interacting with hydrophilic choline and/or phosphate heads, we can follow in Figures 4-8, the progress of attractive interactions that favor the nanorod taking a position parallel to the plane of the membrane, during the permeation process shown in the corresponding cartoons in Figure 3(a)-(e).

We now report the details (Figure 5) of a typical mechanism of permeation of the PEGylated gold nanorod (at 10° angle to the membrane normal) in the DPPC lipid bilayer membrane with PEG18-NR at constant velocity of 0.05 m/s. Figure 5 shows that the nanorod axis tends to lie down parallel to the membrane surface *at the same point in the trajectory where the blue hydrophilic patch grows in area*. The nanorod axis begins to straighten up along the normal as the ligands on the nanorod begin to interact with hydrophilic groups in both the top and bottom leaflet, as seen in the larger areas of blue patches developing. Finally, the axis is nearly along the normal as the nanorod leaves, with the leading end of the nanorod concomitantly losing its blue patches. We observe this tilting and lying down behavior of the axis of the nanorod during the permeation at all velocities (V1-V4), with the only difference being the exit from the membrane, where at higher velocities the nanorod will straighten up earlier in the trajectory as it exits the second leaflet. At lower velocities the nanorod has more time to interact with lipid head groups from both the top and bottom leaflets and thus takes longer to straighten up and leave the membrane.

In Figure 6 and Figure 7, we present molecular snapshots of permeation of the nanorod with initial angle of 45° away from the normal and 90° (parallel to the membrane), respectively. These correspond to the cartoon representations showing the tilting behavior of the axis of the nanorod, in Figure 3(c) and (d), respectively.

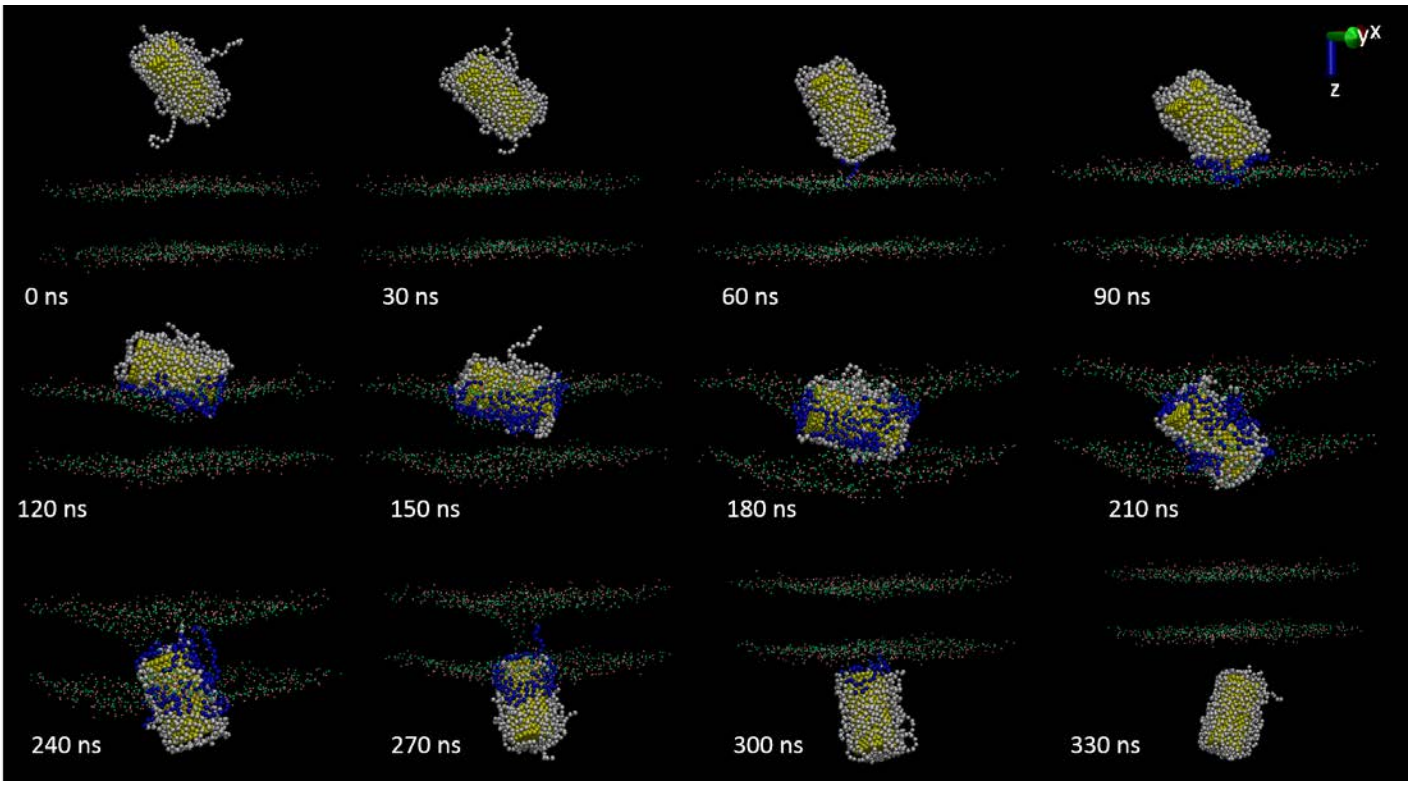

Figure 6. Molecular snapshots of permeation of PEG18-NR in the lipid bilayer membrane at V1=0.05 m/s and initial angle of A2 = 45° where pink=choline, green=phosphate, yellow= AuNR core, white= PEG18-SH ligands, and blue= PEG18 beads within 1.0 nm of choline and phosphate molecules. The cartoon in Figure 3(c) shows this particular trajectory.

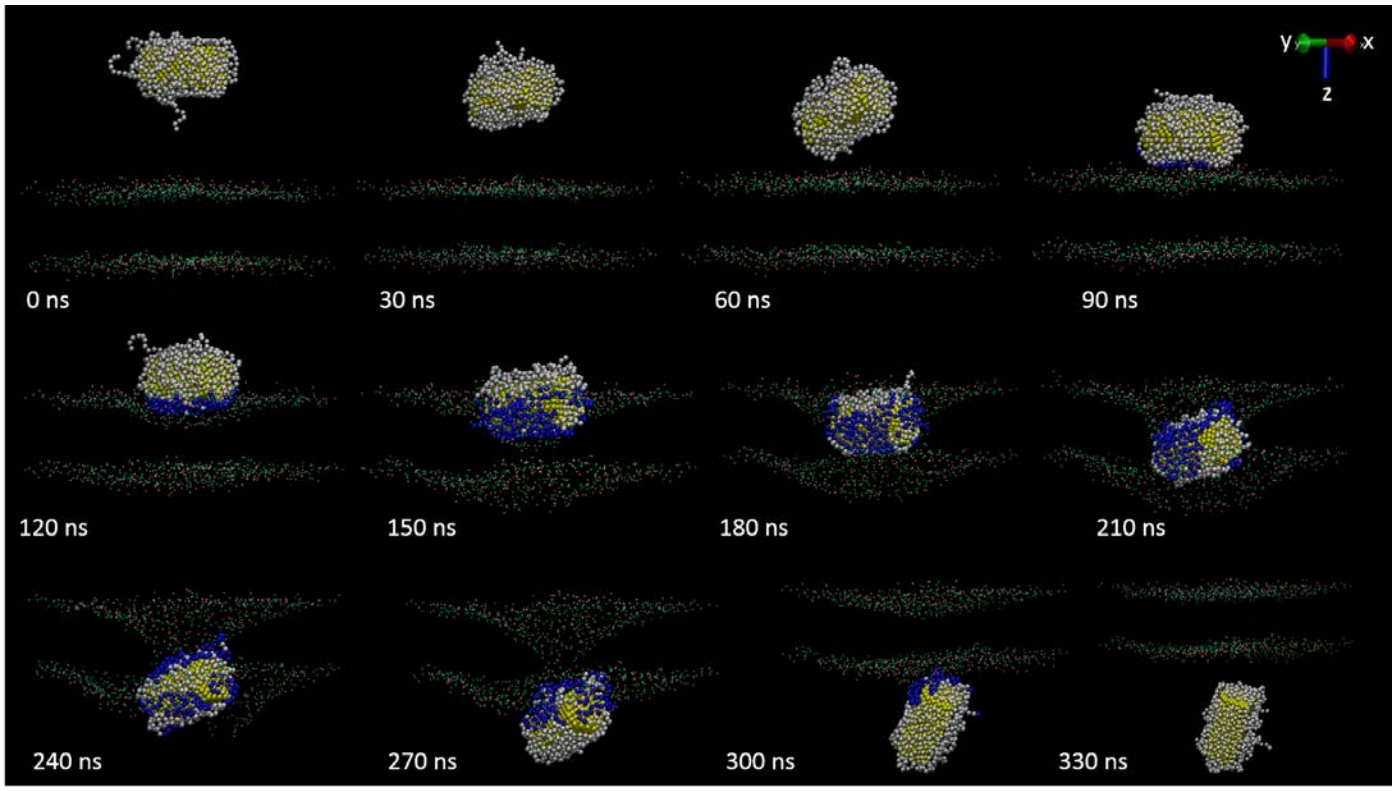

Figure 7. Molecular snapshots of permeation of PEG18-NR in the lipid bilayer membrane at V1=0.05 m/s and initial angle of A3 = 90° where pink=choline, green=phosphate, yellow= AuNR core, white= PEG18-SH ligands, and blue= PEG18 beads within 1.0 nm of choline and phosphate molecules. The cartoon in Figure 3(d) shows this particular trajectory.

For the permeation with initial angle of 45° from the normal to the surface, we see in Figure 6 that the nanorod begins to tilt toward the membrane surface even before permeating the first bilayer leaflet. The attractive interactions between the PEG18 beads and the phosphate and choline head groups causes the nanorod to lie in such a way that a large number of PEG18 beads (blue patches) are interacting with the lipid head groups. We see this also in Figure 6 where the leading PEG18 ligands begin to interact with the first bilayer head groups even before permeation of the top leaflet occurs. We see in both examples in that the PEGylated nanorod will straighten out before exiting the second membrane leaflet, as shown in the cartoons of Figure 3(c) and 3(d), respectively.

For nanorods permeating with initial angle of 45° or higher, we see in both sets of snapshots (Figure 6 and Figure *7*) that once the PEG beads on the nanorod start to interact with the lipid head groups, the nanorod will immediately lie down along the membrane

surface to allow a larger number of lipid heads and PEG beads to experience favorable hydrophilic interactions, as seen in the larger patches of blue on the nanoparticle. The increasing area of blue patches accompanying the nanorod axis lying parallel to the membrane clearly indicates that the change in orientation of the nanorod axis is driven in part by the hydrophilic interactions of the ligand with the phosphate and choline groups of the lipids.

We now consider molecular snapshots from Figure 4 of the permeation pathway of a PEGylated nanorod given no initial tilt angle. We choose to examine this case last, given that a nanorod with no initial tilt angle is the least likely case where many nanorods are penetrating a single membrane at a variety of entry angles. The cartoon in Figure 3(a) shows that even when the nanorod axis starts out not at all tilted from the normal, the sequence of changes in orientation occurs nonetheless. With the thermal fluctuations in individual ligand positions, any ligand that gets close to the membrane surface can attractively interact with the choline and phosphate head groups, thereby breaking the symmetry and initiating a tilt toward a particular direction. When this happens, it brings the ligands closer to the choline and phosphate groups, engendering additional tilting, as indicated by growing areas of blue patches. Therefore, even when the nanorod axis starts out at 0° from the normal, this sequence of events makes the orientation go in favor of increasing hydrophilic interactions (i.e., axis parallel to the membrane surface). Even when starting from 0°, the cartoon in Figure 3(a) shows a marked similarity with Figure 3(b), (c), and (d). Thus, even in the case where the PEGylated nanorod is given no initial angle, the nanorod will still follow the same pathway of permeation; tilting toward the membrane surface, lying down and then slowly moving to straighten out before exiting the membrane.

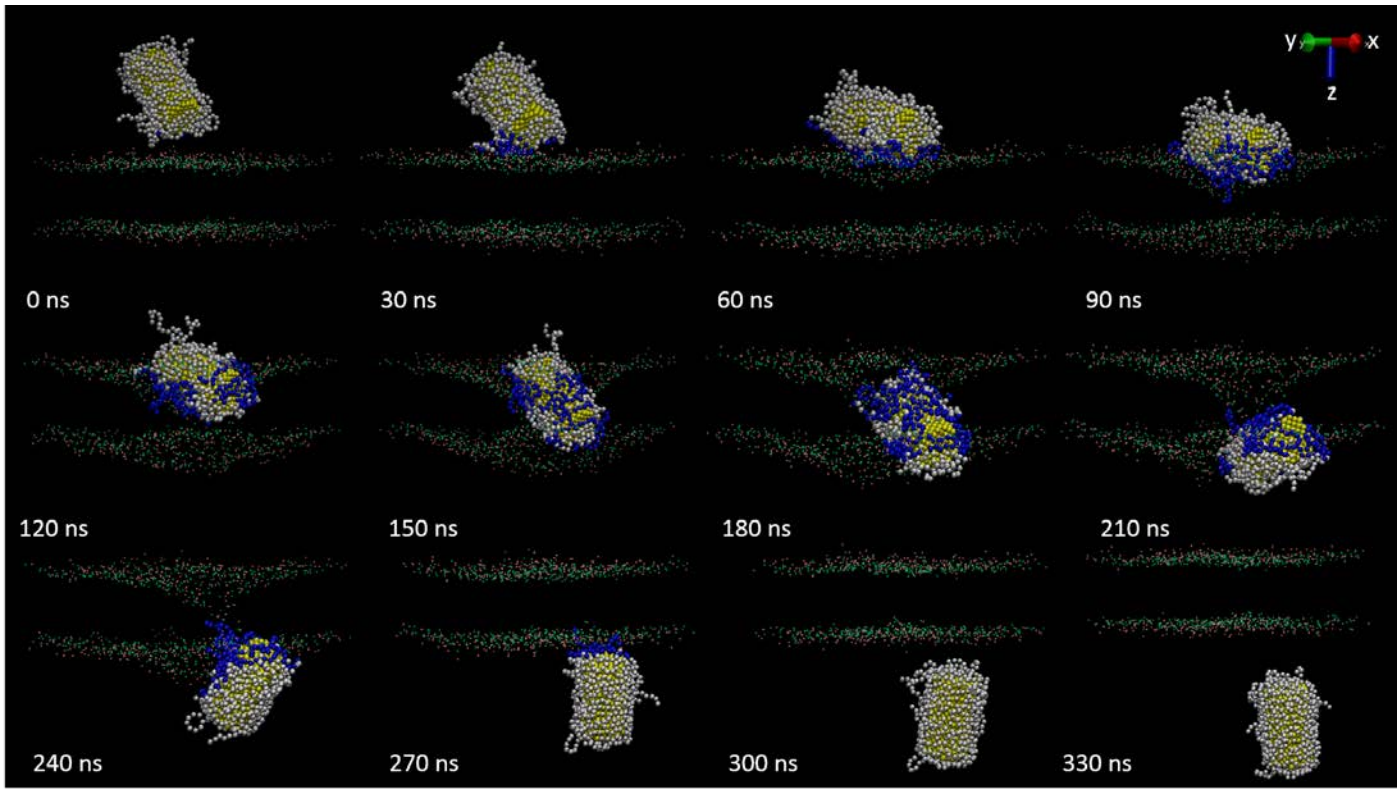

Figure 8. Molecular snapshots of permeation of PEG12-NR in the lipid bilayer membrane at V1=0.05 m/s and initial angle of B2 = 45° where pink=choline, green=phosphate, yellow= AuNR core, white= PEG12-SH ligands, and blue= PEG12 beads within 1.0 nm of choline and phosphate molecules. The cartoon in Figure 3(e) shows this particular trajectory.

In Method (B), we study permeation of the PEGylated AuNR by pulling the center-of-mass at a constant velocity such that the velocity vector maintains the angle of 45° relative to the membrane normal (or z-axis). We label this B2 (same initial tilt angle of 45° as A2). In Figure 2(e), we show the angle of the nanorod relative to the z-axis along the course of permeation for three independent simulations for case B2. In Figure 3(e), we see that the nanorod lies flat on the surface of the lipid heads as soon as the permeation begins. As the permeation continues, the nanorod turns to straighten out and exit the membrane in the same manner as the other cases A0-A3. Figure 8 is a series of molecular snapshots similar to Figure 6, except that here the velocity vector pulling the nanorod is at 45° relative to the normal of the membrane plane. In this case as well, the nanorod maintains a motion that allows it to maximize contacts with the lipid head groups in favorable hydrophilic interactions as seen in the blue patches. Similar to cases A0-A3, the nanorod lies down

parallel to the membrane surface and eventually when exiting, straightens up forming an angle close to 180°, as seen in Figure 2(e). In Method (B2), the straightening of the nanorod occurs 1.5x faster compared to all cases of Method (A) since the nanorod lies down on the membrane surface after 60 ns compared to all cases in Method (A) where the nanorod lies down after 90 ns. This is because the velocity vector in part facilitates such a rotation. Figure 2(e) shows that the nanorod moves through an angle close to 180° upon exit and in some cases, will continue the permeation pathway (after penetrating the second membrane leaflet) in a lying down position. This occurs due to the pulling of the nanorod at a velocity vector at an angle close to 45° relative to the membrane normal. For the same reason, the exit angle for this case is more consistently 180°, unlike the other cases where the exit angle can be 0° or 180°.

In looking at Figures 4-7, we should notice that there is significant disruption of the phosphate and choline positions in both top and bottom leaflets observed in the frames from 120 ns to 300 ns during the time that the nanorod is in transit through the membrane; the z-positions of these lipid groups indicate a wider spread of values compared to the equilibrated membrane before adsorption of the nanorod. Also, we note that after the nanorod has exited, in the 330 ns frame, the choline and phosphate positions have already reverted back to the equilibrium starting positions. We find this in all cases from Method (A) (Figures 4-7). In Method (B) (Figure 8), the disruption of the choline and phosphate groups occurs earlier because the nanorod lies down immediately, and the phosphate and choline groups return to equilibrium by 300-330 ns.

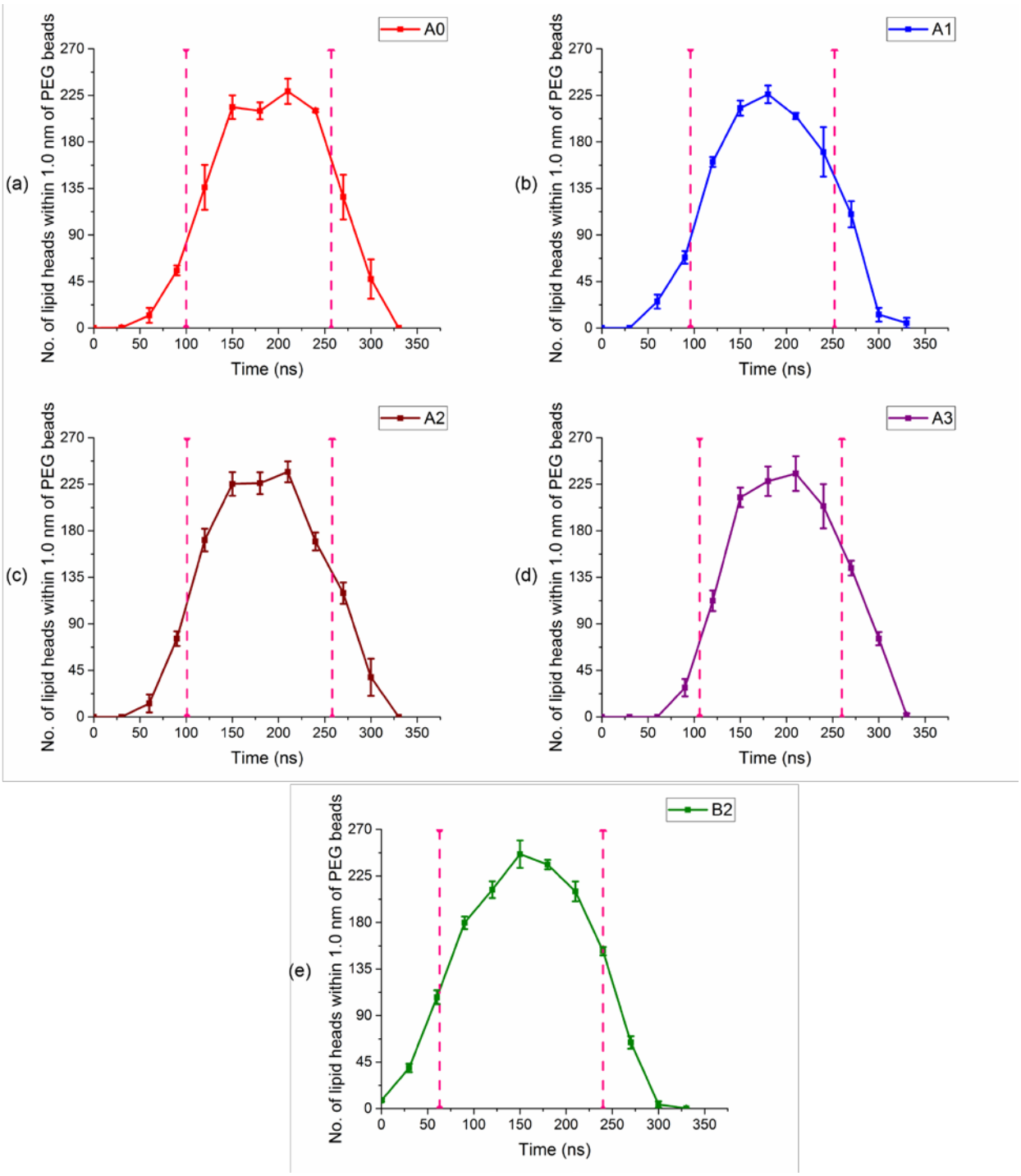

Figure 9. Number of PEG beads within 1.0 nm of phosphate and choline head groups on DPPC lipid bilayer membrane along the course of nanorod permeation under initial angles and Method (a) A0, (b) A1, (c) A2, (d) A3 and (e) B2. Each simulation was carried out with a PEG18-NR (for 9(a), 9(b), 9(c), and 9(d)) and a PEG12-NR (for 9(e)) with velocity of V1= 0.05 m/s and each data point has error bars incorporated based on three independent simulations. The pink dashed lines represent the time when the center-of-mass of the PEGylated nanorod is 2.0 nm above from the top membrane leaflet and later, when it is 2.0

nm below the bottom membrane leaflet; these are the same pink dashed lines from Figure 2.

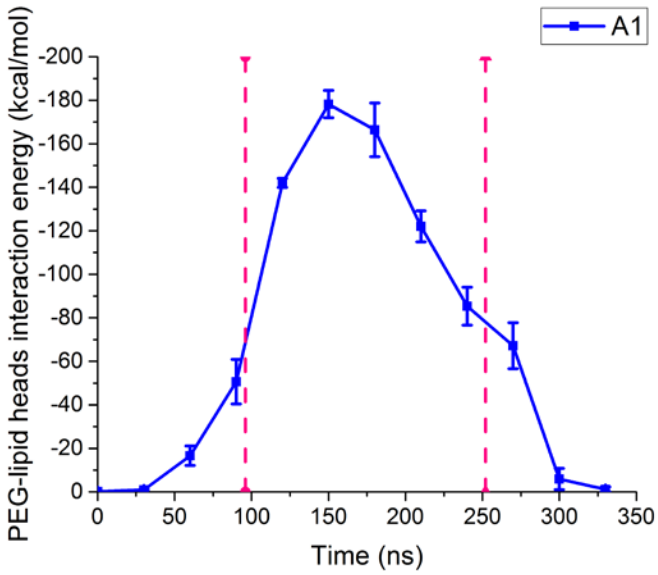

Figure 10. Total interaction energy between all PEG beads and phosphate and choline lipid head groups along the course of nanorod permeation under initial angle of Method A1 = 10°. Each data point has error bars incorporated based on three independent simulations. The pink dashed lines represent the time when the center-of-mass of the PEGylated nanorod is 2.0 nm above from the top membrane leaflet and later, when it is 2.0 nm below the bottom membrane leaflet; these are the same pink dashed lines from Figure 2 and Figure 9.

The consistencies in the changes of the blue patches along the permeation pathway that we have noted for the various entry angles are more easily seen by averaging over several trajectories for each entry angle. We show in Figure *9*, a quantitative view of the number of PEG18 beads within 1.0 nm of the phosphate and choline head groups of the DPPC lipid molecules as the nanorod permeates the lipid membrane in cases of Method (A) and Method (B) averaged over several simulations. We observe that the number of PEG18 beads interacting closely with phosphate and choline head groups remains consistent over a period of about 150 ns from when the nanorod has begun the "engulfing" stages up to when it has begun the "releasing" stages. The lack of a sharp decrease in favorable interactions along the course of the permeation demonstrates that the nanorod continuously positions itself to maximize interactions with the lipid head groups while

permeating the membrane. We denote by two pink dashed lines in Figure *9*, just as in Figure 2, the approach of the nanorod to the lipid membrane and the release of the nanorod after passing the second membrane leaflet, respectively. We now associate the tilt angles in Figure 2, with the number of favorable interactions in Figure 9: The tilt angle increased after the time of the first pink dashed line, which is concomitant with larger number of interactions between PEG beads and phosphate and choline head groups in Figure *9*. After the time of the second pink dashed line, the straightening of the nanorod upon exit (the tilt angle became 0° or 180°) is accompanied by fewer interactions between PEG beads and the hydrophilic lipid head groups. From Figure *9*(a)-(d), it is clear that the average number of PEG beads interacting with the nanorod are similar for all entry angles of Method (A). In Figure *9*(e), the number of lipid head beads interacting closely with the PEG12-NR are slightly higher than the average in Figure *9*(a)-(d) due to the larger total number of ligands on the PEG12-NR compared to the PEG18-NR (corresponding to the higher coverage density of 0.88 ligands/nm^2 for PEG12-NR, whereas PEG18-NR has 0.56 ligands/nm^2), allowing more favorable hydrophilic interactions to occur.

The rotational behavior of the nanorod during permeation of the lipid membrane occurs at all velocities and allows the top leaflet of the membrane to start to recover while the nanorod is exiting the membrane. We also note that as the nanorod passes within the membrane interior, the PEG ligands tend to stay close to each other flattening against the nanorod instead of interacting with the lipids, so as to minimize the unfavorable interaction between the hydrophilic PEG ligands and hydrophobic lipid tails. This permits the lipid heads from the top leaflet to return to their equilibrium position. Upon exit, the nanorod begins to straighten out (as seen in the examples in Figure 3); in all cases, the nanorod exits the membrane after straightening out, irrespective of the initial entry angle, at all velocities.

The interaction energy between the PEG beads and phosphate and choline head groups from the top and bottom leaflets of the lipid bilayer membrane do indeed follow the same profiles as in Figure *9*. As an example, in Figure 10 we show this calculated interaction energy along the course of nanorod permeation for initial angle of Method A1 = 10°. We can see that this follows a similar profile as in Figure *9*(b) where the highest interaction energy occurs at 180 ns when the nanorod is in the middle of the membrane

and PEG beads are interacting with both leaflets of the bilayer membrane. Thus, we have shown that the rotational behavior of the PEGylated NR, lying down and straightening up in the process of permeation, is driven by the attractive interactions between the PEG and the phosphate and choline groups.

Our molecular simulations are of direct penetration of a membrane by diffusion, permeation, and pore formation, involving only non-specific interactions. A completely different pathway of internalization and translocation through a membrane is the process called endocytosis. It is interesting to note that a similar rotational behavior (termed "laying (*sic.*) down to stand up") of a spherocylindrical nanoparticle has been observed in simulations of the sequence of events in the endocytosis process of docking, recognition and binding of the ligands on the NP to the complementary receptors on the cell membrane surface, wrapping of the NP by the membrane, and completion of internalization [14,88,89,90,91,92]. Huang and co-workers [89] simulated the endocytosis of a spherocylindrical nanoparticles by a lipid membrane having special attraction sites (receptors) as the head beads of a 3-bead lipid, and found that the endocytosis of nanorods with no initial angle to the membrane but with a special attraction site at the tip occurred through a lying-down-then-standing-up pathway which is similar behavior to what we observe in our simulations. These endocytosis simulations assigned relatively large ligand-receptor binding energies of $60k_BT$ and high receptor densities in the membrane. Other endocytosis simulations compare PEGylated AuNP systems with identical nanoparticle surface area but various shapes such as cubic, rod- and disc-like [2,93]. These authors find that spherical nanoparticles exhibit the fastest internalization rate for endocytic uptake by a lipid bilayer using a $H_3(T_5)_2$ (H = hydrophilic, T = hydrophobic) representation of the lipid molecule, and using PEGylated nanoparticles which are coarse-grained by one bead per PEG monomer like ours. When the PEGylated nanoparticles approach the cell surface, the targeting moieties attached to each PEG end recognize the receptors and bind with them, due to the specific ligand-receptor attractive interactions that have been defined in their model. Simultaneously, the lipid bilayer starts to bend and wrap around the PEGylated nanoparticles. Eventually, more and more receptors diffuse into the membrane-bending region and bind with the targeting moieties. This stage is mainly driven by the free energy release from the specific ligand-receptor binding that was built into the system,

accompanied by the large bending of the lipid bilayer. The entry angle is found to play an important role during the internalization process in their study. Nanorods starting at a horizontal docking position internalize in a shorter time than nanorods starting at a perpendicular position since the latter need extra for time to rotate and lie down for the binding of targeting moieties with receptors.

The similarity in the rotational behavior is interesting to note, but endocytosis is a completely different pathway for internalization of nanoparticles than the direct permeation through the lipid bilayer that our simulations depict. Our model indicates that specific receptors may not be necessary to include in a dynamic model in order to observe the rotational behavior that accompany a nanorod during the permeation. Note that this rotation observed in our model is dependent on the choice of ligand (hydrophilic) for our gold nanorod; there would likely be a different pathway observed had a different type of ligand (hydrophobic) been implemented for the nanorod.

4.0 Consequences of PEGylated NR permeation

4.1 Water leakage

Observations from our previous work as well as those from other investigators reveal that nanocarriers permeating from the extracellular to intracellular space can induce defects and pore formation in the membrane, which facilitates water leakage into the hydrophobic membrane interior [94,95]. We have defined water penetration in terms of the number of coarse-grained water molecules, originally present in the top compartment of the lipid bilayer membrane, that are found to have moved into the hydrophobic interior of the membrane by nanoparticle permeation. The highly hydrophobic interior of the lipid membrane is the region extending 0.75 nm in both the +z and –z direction from the center of the lipid bilayer membrane at equilibrium that is composed of the lipid tails. Water molecules located near the phosphate heads at the entrance region of the formed water pore are not counted in the total number of waters leaking into the membrane interior.

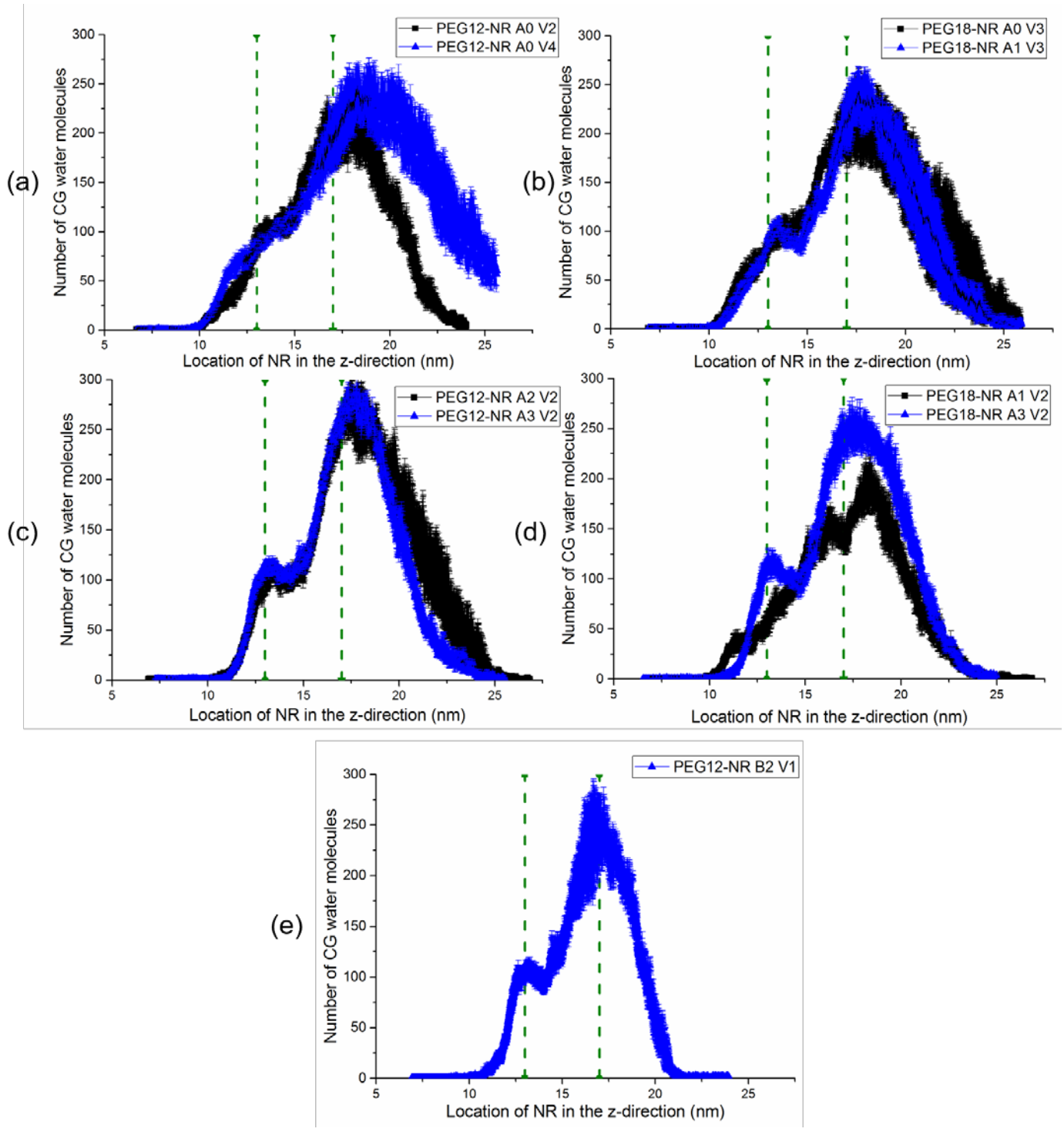

Figure 11. Number of coarse-grained water molecules that permeate into the hydrophobic membrane interior during PEGylated gold nanorod permeation under the following conditions: (a) Effect of nanorod velocity, Effect of changing initial angle from (b) A0 to A1, (c) A2 to A3, and (d), A1 to A3 where A0, A1, A2, and A3 are 0°, 10°, 45°, and 90°, respectively, and (e) water penetration profile for Method (B2). The green dashed lines represent the equilibrated position of the phosphate head groups in the top and bottom

membrane leaflets of the DPPC lipid bilayer membrane. Each data point has error bars incorporated based on three independent simulations.

We now report our observations of water leakage due to PEGylated nanorod permeation under varying conditions of nanoparticle velocity, and initial angle of the nanorod axis. In each case, we have quantified the number of water molecules entering into the hydrophobic membrane interior along the path of the nanorod permeation. In our system, water molecules counted can enter the hydrophobic membrane interior from both the top (1) and bottom (2) membrane compartments in Figure 1. Each data point in Figure 11 has an error bar based on data gathered from three independent simulations; the thicker lines in Figure 11 represent data points of larger error. The green dashed lines represent the equilibrated positions of the phosphate groups in the top and bottom leaflets of the DPPC lipid bilayer membrane. There are differences in water leakage owing to the nature of our system where the functionalized nanorod is allowed to rotate about its center-of-mass during permeation, resulting in a variety of pathways available to the nanorod.

From Figure 11(a), with increasing nanorod velocity, we observe the number of water molecules entering the interior of the membrane for case A0 to increase after the nanorod has exited the lower leaflet of the membrane. We also found this to be the case with the spherical PEGylated gold nanoparticle when comparing water leakage at increasing nanoparticle velocities. During the first part of permeation, while the nanorod is passing the first membrane leaflet, water leakage is nearly velocity-independent. Upon exit, however, nanorods traveling at higher velocities will cause increased disturbance to the lower leaflet of the membrane and recovery of the membrane will be slower. In our work, complete membrane recovery corresponds to that situation when the membrane has zero water molecules found in its hydrophobic membrane interior. At high velocities the water pore formed will survive for longer times and more water molecules can enter the membrane interior. Nevertheless, the membrane eventually expels all the water molecules.

In examining the effect of varying the entry angle on water leakage, we see in Figure 11(b) and Figure 11(c) that water penetration is not sensitive to a difference in entry angle between 0° and 10° and between 45° and 90°. We observed in the snapshots in Figure 4

and Figure *5* that the PEGylated nanorod at initial angle of 0° and 10° take on a similar path during permeation of the lipid membrane. This is the case also when comparing the PEGylated nanorod at initial angle of 45° and 90° where similar paths are identified. We observed a difference between initial angles 10° and 90° in permeation path leading to a noticeable difference in number of water molecules found in the membrane interior. We find that the number of water molecules leaking into the membrane interior increases with increasing nanorod entry angle beyond 45°. At initial angles of 45° and larger, a larger water pore is formed which allows more water molecules to enter the membrane interior. In the end, all water molecules are expelled.

In Figure 11(b, c) and most significantly in Figure 11(d), we see a slight decrease in water penetration along the course of nanorod permeation when the nanorod has passed the first membrane leaflet, particularly at initial angles of 45° and higher. This is unlike the case of the spherical PEGylated gold nanoparticle where water penetration constantly increased until the nanoparticle exited the second leaflet of the membrane. In the water leakage profiles from Figure 11(c) and Figure 11(d), we observe water molecules to exit the membrane instead of continuing to permeate along with the nanorod. For nanorods with large initial angle, there is a tendency (as seen in Figures 6-8) for the nanorod to lie down on its side even before entering the membrane. Therefore, we believe the initial decrease of water in the membrane is partly due to the lying down PEGylated nanorod occupying a large area at the surface of the membrane, effectively blocking additional water molecules from entering the membrane. In Figure 11, we chose to present data at specific velocities and entry angles to represent the overall effect of nanorod velocity and entry angle on water penetration. For instance, from Figure 11(b) and Figure 11(c), the observation that water leakage is not sensitive to entry angles between 0° and 10° and 45° and 90° hold at velocities other than the ones displayed. From Figure 11(d), the observation that water leakage increases for increasing entry angle holds when comparing water penetration in Method (A0) to Method (A3); this observation holds for other velocities than the one displayed in Figure 11(d) however the slight decrease in water leakage due to the nanorod lying down is more prominent at lower permeation velocities.

In the water penetration profile from Figure 11(e), we see a slight decrease as well in water molecules entering the membrane as the nanorod permeates the first leaflet of the

membrane; the profile is quite similar to Figure 11(c) and Figure 11(d). As shown in snapshots from Figure 8, the nanorod lies down parallel to the surface of the membrane again occupying a larger volume of inside the hydrophobic membrane interior and blocking additional water molecules from entering the hydrophobic membrane interior. We can see from all the water leakage profiles in Figure 11 that despite differences of these profiles compared to spherical PEGylated nanoparticles, water molecules will enter the hydrophobic region but ultimately exit the membrane due to recovery of the bilayer leaflets; no permanent damage to the membrane is sustained especially at lower permeation velocities.

When we tracked the compartments into which the water molecules eventually went, we found that of the 300 or so CG waters that entered the middle region of the membrane, all but 5 or so did return back to their original compartment, for all entry angles at the lower pulling velocities. For the highest velocity, all but 20 or so CG waters did not return to their original compartment after entering the hydrophobic membrane interior. In other words, hardly any waters transported across the membrane to the other side during PEGylated nanorod permeation. We did not investigate ion transport for nanorods, but we have already seen from our previous work that this occurs to any significant extent only when the water pore is large and/or long-lived.

4.2 Lipid flip-flops from either leaflet, but no displacement

Lipid flip-flop is considered a biological activity intrinsic to lipid membranes and supported either by integral and transmembrane proteins or in some cases unique enzymes known as flippases that can catalyze the lipid translocation process [96]. For instance, it has been observed experimentally that certain transmembrane peptides such as Gramicidin A can accelerate and facilitate the translocation of lipids through membrane pores [97,98]. Lipid bilayer membranes inside and outside leaflets in nature are asymmetric. Particular lipid compositions are unique to the identity of the membrane and also include many proteins and other biologically relevant molecules like cholesterol [99]. Consequently, unintentional incidences of lipid translocation can affect the process of

molecular recognition at the outer leaflet, or extracellular cell surface; this can have negative effects on cell lifetime and cause cell cytotoxicity [100].

In Figure 12, we show snapshots of typical lipid flip-flop events where lipid molecules move from the top to the bottom membrane leaflet at various initial angles of entry of the PEGylated nanorod including Method (B2) shown in Figure 12(e).

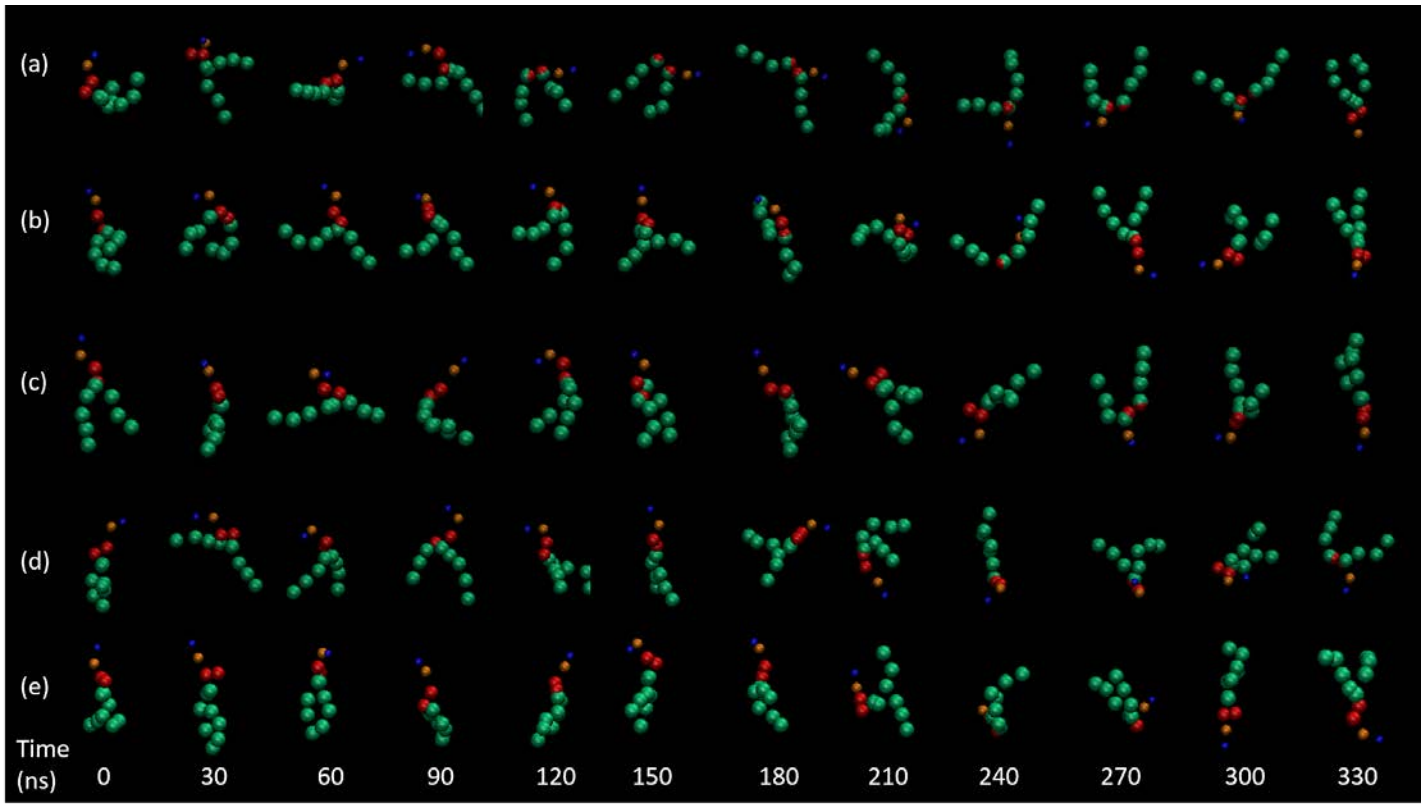

Figure 12. Snapshots of lipid flip-flop events with a PEG12-NR with permeation velocity of V1= 0.05 m/s and initial angle of (a) A0 = 0°, (b) A1 = 10°, (c) A2 = 45°, (d) A3 = 90°, and (e) B2 = 45° (blue = choline, orange = phosphate, red = glycerol, and green = lipid tails).

We see in all of these molecular snapshots, lipid flip-flop events occur by means of the lipid molecule undergoing a full reorientation (in the z-direction) from the top bilayer leaflet to join the bottom leaflet of the membrane. We observed this similar mechanism in the case of permeation with an alkanethiol-coated [33] and PEGylated spherical gold nanoparticle [34]. This suggests that the shape of the nanocarrier does not affect the mechanism by which lipid molecules translocate; at worst, lipid molecule tails alternate open and closed forms while completing the flip-flop. From the snapshots, we also deduce that neither the angle of entry of the nanorod nor the method of pulling at constant velocity

or a constant velocity vector affects the mechanism of lipid translocation; in all cases, lipid molecules that flip-flop will undergo a full reorientation to join the bottom leaflet of the membrane.

We observed, overall, that the number of lipid flip-flop events to increase with initial angle of the nanorod relative to the membrane surface for both the PEG12-NR and PEG18-NR (where the number of events for PEG18-NR are shown in Figure 13). This is more significant as the permeation velocity increases and greater disturbances to the lipid membrane occur. As seen in Figures 6-8, when the entry angle of the PEGylated nanorod is large, the nanorod tends to rotate and lie down on the top leaflet of the membrane before permeating into the membrane interior. This disturbs lipid molecules and results in large numbers of lipid molecules displacing from the top leaflet to interact with the PEG ligands. As the nanorod continues the permeation, the lipid molecules that displaced far enough from the top leaflet join the lower leaflet as the nanorod exits the membrane; this contributes to the number of flip-flop events in. For the lowest permeation velocities, the number of lipid flip-flop events is small, less than 3% of total lipids in the membrane, switched to the other leaflet during permeation of the nanorod.

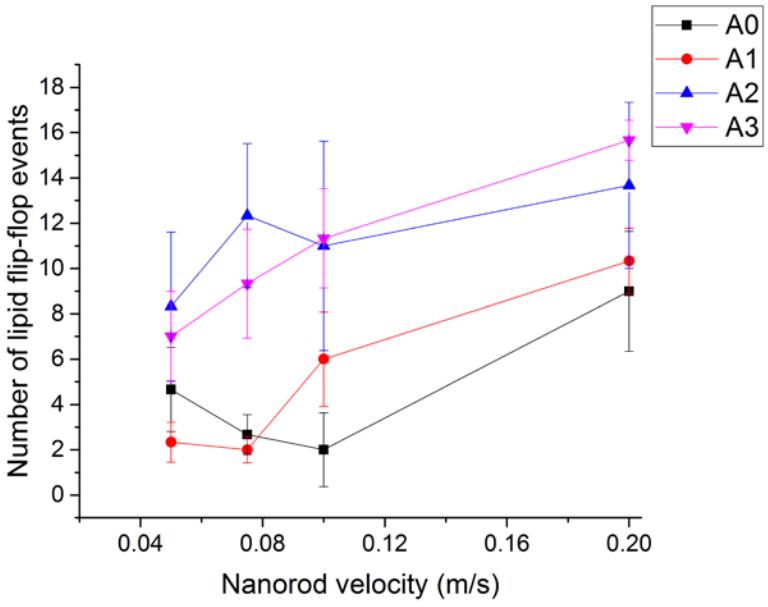

Figure 13. Number of lipid flip-flop events with a PEG18-NR with permeation velocity of V1= 0.05 m/s and varying entry angle. Each data point has error bars incorporated based on three independent simulations.

In our previous work on permeation with alkanethiol-coated gold nanoparticles [33], we observed few lipid molecules to complete lipid flip-flop; instead, a majority of lipid molecules displaced from the top layer of the membrane and became permanently removed from the membrane by being entangled in the alkanethiol ligands and subsequently carried into the bulk solution. We found that loss of lipid molecules from the membrane occurred due to specific groups of alkanethiol ligands competing with the lipid membrane for favorable hydrophobic interactions with the lipid tails. For PEGylated nanoparticles in the present study, as well as in the case of permeation by spherical PEGylated nanoparticles [34], we observe few to no instances of lipid displacement as a result of nanorod permeation. The less favorable interaction between the hydrophilic ligands and hydrophobic lipid tails does not allow for close association and interaction between them during the permeation, thus, lipid molecules displaced from the top leaflet rejoin the lower leaflet of the membrane after the nanorod has begun to exit the membrane; the net effect is no lipid loss from the membrane.

5.0 Conclusion

In this study, we have explored the mechanism of permeation of PEGylated gold nanorods through a model DPPC lipid bilayer membrane. We observed that this proceeds by lying down and then straightening up while leaving regardless of the initial entry angle of the nanorod axis relative to the membrane surface. We show that the lying down behavior maximizes the attractive interactions between the hydrophilic PEG ligand and the hydrophilic phosphate and choline groups of the lipid. New experimental imaging methods utilizing orientation and rotational tracking of nanoparticles now make it possible to simultaneously visualize, with nanometer precision, a single gold nanorod in a live cell. The tracking allows position localization and determination of the orientation and rotational motion of the gold nanorod utilizing microscopy to take images, in differential interference contrast mode, simultaneously with the bright field modes [101]. In another new experimental imaging technique, direct observation of a transmembrane event where (a) negatively charged gold nanorods approaching the plasma membrane from the open

solution, (b) being confined rotationally and laterally static at a membrane site (with a narrow distribution of angles close to perpendicular to the membrane surface), and (c) the exact moment of the nanorod detaching from the inner surface of the membrane was captured in a movie [102]. The method used annular oblique illumination, positioning the focal plane of the microscope objective at the sidewall of the cell, with a birefringent prism to split the AuNR plasmonic scattering into two channels of polarization, thereby providing azimuthal and polar angles. This experimental method permits monitoring of the distribution of angles (Θ, ϕ) the gold nanorod axis makes relative to the membrane surface. Our simulations display the results that would be observed if these two experimental methods were used on a model planar membrane tethered to a solid support.

It is interesting that simulations of endocytosis of a nanorod with strong attractor sites on its surface also exhibit a lying down on a receptor-loaded lipid layer prior to wrapping; our simulations of direct permeation require no specific strong interaction sites on the particle nor specific receptors on the lipid. Our coarse-grained system includes articulated mobile ligands with non-specific interactions with a lipid membrane where various components of the lipid molecules are represented. In a way, maximizing the coupling of the attractive surface sites on the spherocylindrical particle to the receptors on the membrane in the endocytosis model provides a similar driving mechanism for their lying down and wrapping.

We found, similar to our simulations with a PEGylated gold nanoparticle, few to no lipid molecules are removed from the membrane due to permeation. We found permanent effects of water leakage, with the membrane recovering consistently after the nanorod has exited the membrane and the water molecules expelled back to their original compartment. The results of this study may be of interest to those experimentalists studying drug delivery who may find the permeation pathway of the nanorod significant to a specific application of drug delivery method in its discovery phase.

AUTHOR INFORMATION

*Email: murad@iit.edu. Phone: (312)- 567-3867

Notes

The authors declare no competing financial interest.

ACKNOWLEDGEMENTS

This research has been funded by a grant from the National Science Foundation (Grant No. CBET-1263107/1545560

REFERENCES

[1] A. Albanese, P.S. Tang, and W.C. Chan, Annu. Rev. Biomed. Eng. **14**, 1-16 (2012).
[2] Y. Li, M. Kröger, and W.K. Liu, W. K, Nanoscale. **7**(40), 16631-16646 (2015).
[3] S.M. Loverde, M.L. Klein, and D.E. Discher, Adv. Mater. **24**(28), 3823-3830 (2012).
[4] T. Niidome, M. Yamagata, Y. Okamoto, Y. Akiyama, H. Takahashi, T. Kawano, and Y. Niidome, J. Control. Release. **114**(3), 343-347 (2006).
[5] J.C.Y. Kah, K.Y. Wong, K.G. Neoh, J.H. Song, J.W.P. Fu, S. Mhaisalkar, and C.J.R. Sheppard, J. Drug. Target. **17**(3), 181-193 (2009).
[6] J.V. Jokerst, T. Lobovkina, R.N. Zare, and S.S. Gambhir, Nanomedicine. **6**(4), 715-728 (2011).
[7] N. Khlebtsov, L. Dykman, Chem. Soc. Rev. **40**(3), 1647-1671 (2011).
[8] C.H. Wang, C.J. Liu, C.C. Chien, H.T. Chen, T.E. Hua, W.H. Leng, T.C. Lai, Mater. Chem. Phys. **126**(1), 352-356 (2011).
[9] X. Huang, P.K. Jain, I.H. El-Sayed, and M.A. El-Sayed, Nanomedicine, **2**(5), 681-693 (2007).
[10] C.H. Wang, C.J. Liu, C.L. Wang, T.E. Hua, J.M. Obliosca, K.H. Lee, and J.H. Je, J. Phys. D: Appl. Phys. **41**(19), 195301 (2008).
[11] W. Eck, A.I. Nicholson, H. Zentgraf, W. Semmler, and S. Bartling, Nano Lett. **10**(7), 2318-2322 (2010).
[12] P. Bailon, and C.Y. Won, Expert Opin. Drug Deliv. **6**(1), 1-16 (2009).
[13] Y.C. Huang, Y.C. Yang, K.C. Yang, H.R. Shieh, T.Y. Wang, Y. Hwu, Y.J. Chen, BioMed Research Inter. Article ID 182353, (2014)
[14] H.M. Ding, and Y.Q. Ma, Small, **11**(9-10), 1055-1071 (2015).
[15] C. Carnovale, G. Bryant, R. Shukla, and V. Bansal, Progress in Materials Science, 83, 152-190 (2016).
[16] M.A. El-Sayed, A.A. Shabaka, O.A. El-Shabrawy, N.A. Yassin, S.S. Mahmoud, S.M. El-Shenawy, and N. Salah, PloS one. **8**(10), e76207 (2013).
[17] G. von Maltzahn, J.H. Park, A. Agrawal, N.K. Bandaru, S.K. Das, M.J. Sailor, and S.N. Bhatia, Cancer Res. **69**(9), 3892-3900 (2009).
[18] G. von Maltzahn, A. Centrone, J.H. Park, R. Ramanathan, M.J. Sailor, T.A. Hatton, and S.N. Bhatia, Adv. Mat. **21**(31), 3175-3180 (2009).
[19] Y.Y. Yu, and S.S. Chang, C.L. Lee, C.C. Wang, J.Phys.Chem.B. **101**(34), 6661-6664 (1997).
[20] S. Link, M.B. Mohamed, and M.A. El-Sayed, J.Phys.Chem.B. **103**(16), 3073-3077 (1999).
[21] H.T. John, Chem. Commun. (31), 3924-3926 (2005).
[22] S. Eustis, and M. El-Sayed, J.Phys.Chem.B. **109**(34), 16350-16356 (2005).
[23] A.V. Alekseeva, V.A. Bogatyrev, L.A. Dykman, B.N. Khlebtsov, L.A. Trachuk, A.G. Melnikov, and N.G. Khlebtsov, Appl. Opt. **44**(29), 6285-6295 (2005).
[24] J. Zhu, L. Huang, J. Zhao, Y. Wang, Y. Zhao, L. Hao, and Y. Lu, Mater Sci Eng B. **121**(3), 199-203 (2005).
[25] H. Wang, T.B. Huff, D.A. Zweifel, W. He, P.S. Low, A. Wei, and J.X. Cheng, Proc. Natl. Acad. Sci. U.S.A. **102**(44), 15752-15756 (2005).
[26] G. von Maltzahn, J.H. Park, A. Agrawal, N.K. Bandaru, S.K. Das, M.J. Sailor, and S.N. Bhatia, Cancer Res. **69**(9), 3892-3900 (2009).
[27] K. Y Lin, A. F. Badgley, A.Y. Zhang, D.L. Karl, S.S. Yoon, and S.N. Bhatia, Nano Life, **1**(03n04), 277-287 (2010).
[28] X. Huang, I.H. El-Sayed, W. Qian, and M.A. El-Sayed, J. Amer. Chem. Soc, **128**(6), 2115-2120 (2006).
[29] L.M. Maestro, E. Camarillo, J.A. Sánchez-Gil, R. Rodríguez-Oliveros, J. Ramiro-Bargueño, A.J. Caamaño, and D. Jaque, RSC Adv. **4**(96), 54122-54129 (2014).
[30] T. Niidome, M. Yamagata, Y. Okamoto, Y. Akiyama, H. Takahashi, T. Kawano, and Y. Niidome, J. Control. Release. **114**(3), 343-347 (2006).
[31] K.Y Lin, A. F. Badgley, A.Y. Zhang, D.L. Karl, S.S. Yoon, and S.N. Bhatia, Nano Life, **1**(03n04), 277-287 (2010).
[32] A.F. Bagley, S. Hill, G.S. Rogers, and S.N. Bhatia, ACS Nano. **7**(9), 8089-8097 (2013).
[33] P.A. Oroskar, C.J. Jameson, and S. Murad, Langmuir. **31**(3), 1074-1085 (2015).
[34] P.A. Oroskar, C.J. Jameson, and S. Murad, Langmuir. **32**(30), 7541-7555 (2016).
[35] K.S. Soppimath, T.M. Aminabhavi, A.R. Kulkarni, and W.E. Rudzinski, J. Control. Release. **70**(1), 1-20 (2001).

[36] P. Ghosh, G. Han, M. De, C.K. Kim, and V.M. Rotello, Adv Drug Deliver Rev. **60**(11), 1307-1315 (2008).
[37] D. Pissuwan, T.Niidome, and M.B. Cortie, J. Control Release. **149**(1), 65-71 (2011).
[38] H. Yuan, C.J. Jameson, and S. Murad, Mol. Phys. **108**(12), 1569-1581 (2010).
[39] B. Song, H. Yuan, C.J. Jameson, and S. Murad, Mol. Phys. **110**(18), 2181-2195 (2012).
[40] A.K. Sum, R. Faller, and J.J. de Pablo, Biophys. J. **85**(5), 2830-2844 (2003).
[41] S. Leekumjorn, and A.K. Sum, Biophys. J. **90**(11), 3951-3965 (2006).
[42] R. Veldhuizen, K. Nag, S. Orgeig, and F. Possmayer, BBA Mol. Basis Dis. **1408**(2), 90-108 (1998).
[43] E. London, J. Biol. Chem. **279**(11), 9997-10004 (2004).
[44] O. Bouffioux, A. Berquand, M. Eeman, M. Paquot, Y.F. Dufrêne, R. Brasseur, and M. Deleu, BBA Mol. Basis Dis. **1768**(7), 1758-1768 (2007).
[45] P.J. Bond, J. Holyoake, A. Ivetac, S. Khalid, M.S. Sansom, J. Struct. Biol. **157**(3), 593-605 (2007).
[46] J.T. Padding, and W.J. Briels, J. Chem. Phys. **117**(2), 925-943 (2002).
[47] E. Choi, J. Mondal, A. Yethiraj, J. Phys. Chem. B. **118(**1), 323-329 (2014).
[48] S. A. Oelmeier, F. Dismer, and J. Hubbuch, BMC Biophys. **5**(1),14 (2012).
[49] K. Prasitnok, and M. R. Wilson, M. R, Phys. Chem. Phys. Chem, **15**(40), 17093-17104 (2013).
[50] S. J., Marrink, H. J. Risselada, S. Yefimov, D. P. Tieleman, and A. H. De Vries, J. Phys. Chem. B. **111**(27), 7812-7824 (2007).
[51] L. Monticelli, S. K. Kandasamy, X. Periole, R. G. Larson, D. P. Tieleman, and S. J. Marrink, J. Chem. Theory Comput. **4**(5), 819-834 (2008).
[52] A.A. Gurtovenko, and I. Vattulainen, J.Phys.Chem.B. **111**(48), 13554-13559 (2007).
[53] B. Song, H. Yuan, S.V. Pham, C.J. Jameson, and S. Murad, Langmuir, **28**(49), 16989-17000 (2012).
[54] E. Panizon, D. Bochicchio, L. Monticelli, and G. Rossi, J. Phys. Chem. B. **119**(25), 8209-8216 (2015).
[55] S.J. Marrink, and D.P. Tieleman, Chem. Soc. Rev. **42**(16), 6801-6822 (2013).
[56] G. Rossi and L. Monticelli, Adv. Phys. X, 1:2, 276-296 (2016).
[57] H. Lee, A.H. de Vries, S. J. Marrink, and R.W. Pastor, J. Phys. Chem. B. **113**(40), 13186-13194 (2009).
[58] H. Lee, and R.W. Pastor, J. Phys. Chem. B. **115**(24), 7830-7837 (2011).
[59] H. Lee, R.M. Venable, A.D. MacKerell, R.W. Pastor, Biophys J. **95**(4), 1590-1599 (2008).
[60] T.M. Nguyen, J. Gigault, V.A. Hackley, Anal. Bioanl. Chem. **406**(6), 1651-1659 (2014).
[61] Y. Qiu, Y. Liu, L. Wang, L. Xu, R. Bai, Y. Ji, and C. Chen, Biomaterials. **31**(30), 7606-7619 (2010).
[62] A. Ghanbari, M. Rahimi, and J. Dehghany, J. Phys. Chem. C. **117**(47), 25069-25076 (2013).
[63] M.K. Corbierre, N.S. Cameron, M. Sutton, S.G. Mochrie, L.B. Lurio, A. Rühm, and R.B. Lennox, J. Am. Chem. Soc. **123**(42), 10411-10412 (2001).
[64] J.S. Smith, D. Bedrov, and G.D. Smith, Compos. Sci. Technol. **63**(11), 1599-1605 (2003).
[65] D. Barbier, D. Brown, A.C. Grillet, and S. Neyertz, Macromolecules. **37**(12), 4695-4710 (2004).
[66] C. Chevigny, F. Dalmas, E. Di Cola, D. Gigmes, D. Bertin, F. Boué, and J. Jestin, Macromolecules. **44**(1), 122-133 (2010).
[67] A.S. Karakoti, S. Das, S. Thevuthasan, and S. Seal, Angew. Chem. Int. Ed. Engl. **50**(9), 1980-1994 (2011).
[68] K. Rahme, L. Chen, R.G. Hobbs, M.A. Morris, C. O'Driscoll, and J.D. Holmes, RSC Adv. **3**(17), 6085-6094 (2013)
[69] X. Xia, M. Yang, Y. Wang, Y. Zheng, Q. Li, J. Chen, and Y. Xia, Y, ACS Nano. **6**(1), 512-522 (2011).
[70] C. Kinnear, H. Dietsch, M.J. Clift, C. Endes, B. Rothen-Rutishauser, and A. Petri-Fink, Angew. Chem. Int. Ed. Engl. **52**(7), 1934-1938 (2013).
[71] J.E. Gagner, S. Shrivastava, X. Qian, J.S. Dordick, and R.W. Siegel, J. Phys. Chem. Lett. **3**(21), 3149-3158 (2012).
[72] E. Oh, K. Susumu, A.J. Mäkinen, J.R. Deschamps, A.L. Huston, and I.L. Medintz, J. Phys. Chem. C. **117**(37), 18947-18956 (2013).
[73] S.A. Oelmeier, F. Dismer, and J. Hubbuch, BMC Biophys. **5**(1), (2012).
[74] B. Song, H. Yuan, C.J. Jameson, and S. Murad, Mol. Phys. **109**(11), 1511-1526 (2011).
[75] D. Lingwood, and K. Simons, Science, **327**(5961), 46-50 (2012).
[76] M.C. Schmidt, B. Rothen-Rutishauser, B. Rist, A. Beck-Sickinger, H. Wunderli-Allenspach, W. Rubas, and H.P. Merkle, Biochem. **37**(47), 16582-16590 (1998).
[77] M. Tanaka, E. Sackmann, Nature. **437**(7059), 656-663 (2005).
[78] J.K. Vasir, and V. Labhasetwar, Biomater. **29**(31), 4244-4252 (2008).
[79] Q. Zeng, A. Yu, and G. Lu, Ind. Eng. Chem. Res. **49**(24), 12793-12797 (2010).

[80] Y. Xiao, H. Hong, V.Z. Matson, A. Javadi, W. Xu, Y. Yang, and D.A. Steeber, Theranostics. **2**(8), 757-768 (2012).
[81] A.M. Alkilany, L.B. Thompson, S.P. Boulos, P.N. Sisco, C.J Murphy, Adv. Drug Deliv. Rev. **64**(2), 190-199 (2012).
[82] R.A. Petros, and J.M. DeSimone, Nat. Rev. Drug Discov. **9**(8), 615-627 (2010).
[83] J. Wang, J.D. Byrne, M.E. Napier, and J.M. DeSimone, Small, **7**(14), 1919-1931 (2011).
[84] A.D. Grief, and G. Richardson. J. Magn. Magn. Mater. **293**(1), 455-463 (2005).
[85] S. Plimpton, J. Comput. Phys. **117**(1), 1-19 (1995).
[86] A.A. Gurtovenko, and I. Vattulainen, Biophys. J. **92**(6), 1878-1890 (2007)
[87] S.E. Gratton, P.A. Ropp, P.D. Pohlhaus, J.C. Luft, V.J. Madden, M.E. Napier, and J.M. DeSimone, Proc. Natl. Acad. Sci. **105**(33), 11613-11618 (2008).
[88] X. Shi, A. von Dem Bussche, R.H. Hurt, A.B. Kane, and H. Gao, Nature Nanotechnol. **6**(11), 714-719 (2011).
[89] C. Huang, Y. Zhang, H. Yuan, H. Gao, and S. Zhang, S, Nano Lett. **13**(9), 4546-4550 (2013).
[90] S. Zhang, H. Gao, G. Bao, ACS Nano. **9**(9), 8655-8671 (2015).
[91] X. Yi, X. Shi, and H. Gao, Nano Lett. 14(2), 1049-1055 (2014).
[92]R. Vácha, F.J. Martinez-Veracoechea, and D. Frenkel, Nano Lett. **11**(12), 5391-5395 (2011).
[93] Y. Li, M. Kröger, and W.K. Liu, Biomater. **35**(30), 8467-8478 (2014).
[94] D.P. Tieleman and S.J. Marrink, J. Am. Chem. Soc. **128**(38), 12462-12467 (2006)
[95] W.D. Bennett and D.P. Tieleman, J. Chem. Theory Comput. **7**(9), 2981-2988 (2011).
[96] D.L. Daleke, J. Biol. Chem. **282**(2), 821-825 (2007).
[97] T.C. Anglin, J. Liu, and J.C. Conboy, Biophys. J. **92**(1), L01-L03 (2007).
[98] K. Matsuzaki, O. Murase, N. Fujii, K. Miyajima, Biochemistry. **35**(35), 11361-11368 (1996).
[99] J.H. Ipsen, O.G. Mouritsen, and M. Bloom, Biophys. J. **57**(3), 405 (1990).
[100] P.F. Devaux, Biochemistry. **30**(5), 1163-1173 (1991).
[101] Y. Gu, G. Wang, and N. Fang, ACS Nano. **7**(2), 1658-1665 (2013).
[102] D. Xu, Y. He, and E.S. Yeung, Anal. Chem. **86**(7), 3397-3404 (2014).